The Journal of Chemical Physics

Ultrafast fs coherent excitonic dynamics in CdSe quantum dots assemblies addressed and probed by 2D electronic spectroscopy

Cite as: J. Chem. Phys. **154**, 014301 (2021); https://doi.org/10.1063/5.0031420
Submitted: 30 September 2020 . Accepted: 11 December 2020 . Published Online: 04 January 2021

Elisabetta Collini, Hugo Gattuso, R. D. Levine, and F. Remacle

The Journal of Chemical Physics ARTICLE scitation.org/journal/jcp

Ultrafast fs coherent excitonic dynamics in CdSe quantum dots assemblies addressed and probed by 2D electronic spectroscopy

Cite as: J. Chem. Phys. 154, 014301 (2021); doi: 10.1063/5.0031420
Submitted: 30 September 2020 • Accepted: 11 December 2020 •
Published Online: 4 January 2021

Elisabetta Collini,[1] Hugo Gattuso,[2] R. D. Levine,[3] and F. Remacle[2,3,a)]

AFFILIATIONS

[1] Department of Chemical Sciences, University of Padova, Via Marzolo 1, I-35131 Padova, Italy
[2] Theoretical Physical Chemistry, RU MOLSYS, University of Liège, Allée du 6 Août 11, B4000 Liège, Belgium
[3] The Fritz Haber Research Center for Molecular Dynamics and Institute of Chemistry, The Hebrew University of Jerusalem, Jerusalem 91904, Israel

Note: This paper is part of the JCP Special Topic on Excitons: Energetics and Spatio-Temporal Dynamics.
[a)] **Author to whom correspondence should be addressed:** fremacle@uliege.be

ABSTRACT

We show in a joint experimental and theoretical study that ultrafast femto-second (fs) electronic coherences can be characterized in semi-conducting colloidal quantum dot (QD) assemblies at room temperature. The dynamics of the electronic response of ensembles of CdSe QDs in the solution and of QD dimers in the solid state is probed by a sequence of 3 fs laser pulses as in two-dimensional (2D) electronic spectroscopy. The quantum dynamics is computed using an excitonic model Hamiltonian based on the effective mass approximation. The Hamiltonian includes the Coulomb, spin–orbit, and crystal field interactions that give rise to the fine structure splittings. In the dimers studied, the interdot distance is sufficiently small to allow for an efficient interdot coupling and delocalization of the excitons over the two QDs of the dimer. To account for the inherent few percent size dispersion of colloidal QDs, the optical response is modeled by averaging over an ensemble of 2000 dimers. The size dispersion is responsible for an inhomogeneous broadening that limits the lifetimes of the excitonic coherences that can be probed to about 150 fs–200 fs. Simulations and experimental measurements in the solid state and in the solution demonstrate that during that time scale, a very rich electronic coherent dynamics takes place that involves several types of intradot and interdot (in the case of dimers) coherences. These electronic coherences exhibit a wide range of beating periods and provide a versatile basis for a quantum information processing device on a fs time scale at room temperature.

I. INTRODUCTION

Small nanometric semi-conducting colloidal quantum dots (QD's) can be assembled into solid state devices that operate at room temperature. In these materials, the confinement effect arising from the nanosize of the dots leads to discrete excitonic levels when the Bohr radius of the exciton is larger than the QD size.[1,2] Colloidal synthesis methods provide a low size dispersion, with the variance of the size distributions of the order of a few percent. The control of excitonic transition energies with the QD size has been exploited since the early days of nanotechnologies.[3,4] The size control, coupled with the control made possible by the capping ligands, has led to a wide variety of applications, ranging from solar cells and photovoltaics to photonics, nonlinear optics, and lasers.[5–9] QD assemblies are also attractive for information processing applications. Earlier proposals were based on spin coupled epitaxially grown QDs.[10,11] Further progress in quantum technologies, i.e., in sensing and information processing, requires the manipulation of coherences between quantum states, preferably at room temperature. Colloidal QD assemblies are promising materials also in this context.[12–14] Recent experimental studies of CdSe QDs in solution and films using two-dimensional electronic (2DES) and fs pump–probe transient absorption spectroscopies have successfully probed fast fs inter-excitonic coherences as well as the ps time scale coherent beating of the LO phonon

mode.[15–21] Several dephasing mechanisms, i.e., ensemble size and capping disorder, geometry fluctuations, trap states, relaxation to the phonon modes and to biexciton states and interaction with the environment, contribute to making the electronic coherence short lived, with typical lifetimes shorter than 100 fs.[15,20,22–29]

In CdSe QDs, the spin–orbit (SO) interactions between the orbital angular momentum of the hole p state (localized on Se) and the spin of the electron split the degeneracies of the exciton. Together with the weaker crystal field and exchange interactions, the SO interactions lead to fine structure bands.[30–35] We have recently reported on inter-excitonic fs coherences in ensembles of isolated, small (2.5 nm–4.5 nm) colloidal size-dispersed CdSe QDs[36] and of QD dimers.[37] Here, we focus on the modeling of the 2D frequency maps that are measured in 2D electronic spectroscopy (2DES). We show that the fine structure bands together with inhomogeneous broadening arising from size dispersion at the level of the ensemble[38] play an essential role in shaping the specific unusual features of the fast beating fs inter-excitonic coherences that are experimentally observed in the 2D response of CdSe QDs.

In Sec. II, we provide a brief outline of the model that we use to describe the excitonic level structure of ensembles of size dispersed isolated QDs and QD dimers with a mean diameter in the range 2.5 nm and 4.5 nm. We use a semi-empirical model based on the $\mathbf{k}\cdot\mathbf{p}$-effective mass approximation[39] and include the effect of spin–orbit coupling and crystal field splittings[30,31,40,41] to get a basis of exciton states for isolated QDs and dimers of QDs (Secs. II A and II B). More details can be found in Refs. 36–38 and 42 and in the supplementary material. This level of description of the electronic structure, while approximate, allows taking into account the role of fine structure states and of size dispersion on the electronic optical response of ensembles of thousands of QDs and QD dimers during the first dozens of fs of the dynamics, before the onset of significant coupling to phonon modes (Sec. II C). In Sec. II D, we summarize our approach based on the nonlinear response function to weak pulses in the impulsive limit[43–46] to compute the 2D maps as probed by a sequence of 3 fs laser pulses. Section III provides a comparison and a characterization of the computed and experimental responses and a discussion.

II. MODELING OF THE 2D MAPS

A. Fine structure levels in isolated QDs

We model the electronic structure of an isolated CdSe QD in the strong confinement limit using the $\mathbf{k}\cdot\mathbf{p}$-effective mass model (EMA) approximation[39] to get the zero order energies and wave functions of the exciton hole–electron pairs. The diameter D of each CdSe QD in the ensemble is drawn from a Gaussian distribution with a mean value, $\bar{D}$, and standard deviation σ: $P(D) = \left(1/\sigma\sqrt{2\pi}\right)\exp\left(-\left(D-\bar{D}\right)^2/2\sigma^2\right)$. In all simulations reported below, the standard deviation, σ, corresponds to 5% of the mean diameter. We assume a spherical confinement potential for the electrons and the holes, with finite depth, $V_{0,e/h}$, which is size-dependent through the empirical relations, taken from Ref. 47: $V_{0e}(D) = 3.49 + 2.47(D)^{-1.32}$ for the electron and $V_{0h}(D) = 5.23 + 0.74(D)^{-0.95}$ for the hole. The one particle Hamiltonian for the hole and the electron envelope states used to build the excitons, therefore, depends on the QD diameter D,

$$H_{D,e/h}\phi^{e/h}_{D,i}(\mathbf{r}) = \left(-\frac{\hbar^2}{2m^*_{e/h}}\nabla^2 + V_{D,e/h}(\mathbf{r})\right)\phi^{e/h}_{D,i}(\mathbf{r}) = E^{e/h}_{D,i}\phi^{e/h}_{D,i}(\mathbf{r}). \tag{1}$$

In Eq. (1), i stands for the index of the hole or the electron wave function. The values of the effective mass for the hole and the electron are $m^*_e = 0.13$ and $m^*_h = 0.82$.[47] The mass of the electron and the hole outside the well is set to 1. To build the exciton basis, we use a minimal basis and retain two hole states and one electron state on each QD. This leads to two excitons per dot whose zero order energies are given by

$$E_m(D) = E^h_{D,i} + E^e_{D,j} + E_{gap}, \tag{2}$$

where $i = 1, 2$ and $j = 1$. E_{gap} is the bandgap of bulk CdSe (=1.75 eV). The $m = 1$ exciton corresponds to the 1S ($i = 1$) state for the hole envelope wave function and a 1S state for the electron one, $\psi_{D,1}(\mathbf{r}_h, \mathbf{r}_e) = \phi^h_{D,1S}(\mathbf{r}_h)\phi^e_{D,1S}(\mathbf{r}_e)$. We label it as the 1S exciton in what follows. $m = 2$ corresponds to the 2S state ($i = 2$) for the hole and the 1S state for the electron, $\psi_{D,2}(\mathbf{r}_h, \mathbf{r}_e) = \phi^h_{D,2S}(\mathbf{r}_h)\phi^e_{D,1S}(\mathbf{r}_e)$. It is labeled the 2S exciton. In both excitons, the electron is in a 1S state. The excitons correspond to singly excited electronic configurations. We obtain three singlets and nine triplets excitons per band for the basis that we use. In CdSe QDs, the 1S and 2S hole states are localized on p ($l = 1$) orbitals of the Se atoms and the electron state on the s ($l = 0$) orbitals of Cd.[30,33,40,41,48] In Se, there is a strong spin–orbit coupling between the orbital angular momentum of the p orbital of the hole and its spin, leading to a splitting of the 1S and 2S hole states into two total angular momentum states, $L = 3/2$ and $L = 1/2$. In the exciton, the angular momentum of the hole state is combined with that of the 1S electron (=1/2) to lead to a total angular momentum F, which can take the values $F = 1$ and 2 for the $L = 3/2$ hole states and $F = 0$ and 1 for the $L = 1/2$ ones. In CdSe QDs, the SO interaction, therefore, splits the two excitons 1S and 2S into four bands of degenerate fine structure exciton states that are labeled as follows: the $1S_{3/2}$ and $2S_{3/2}$ bands are each made of eight degenerate levels (five projection states with $F_z = \pm2, \pm1, 0$ for $F = 2$ and three projection states with $F_z = \pm1, 0$ for $F = 1$). The $1S_{1/2}$ and $2S_{1/2}$ bands are each made of four degenerate levels [three projection states, $F_z = \pm1, 0$, for the $F = 1$ states and 1 ($F_z = 0$) for $F = 0$]. These degenerate states are further split by the crystal field and Coulomb interactions, which lead to a band of 24 fine structure states in total per dot. The eight states of the $1S_{3/2}$ and $2S_{3/2}$ bands split into two sub-bands of five states for which the $F_z = \pm2$ and 0 states are dark and a sub-band of three states that are bright. The four states of the $1S_{1/2}$ and $2S_{1/2}$ bands are bright. We, therefore, obtain four bands of fine structure (FS) states: $1S_{3/2}$, $1S_{1/2}$, $2S_{3/2}$, and $2S_{1/2}$.

Among all interactions, the SO one is by far the largest. We fitted a value of 0.22 eV from experimental data[36] for the range of small QD sizes (diameters from 2.5 nm to 4.5 nm) considered here. This value is smaller than the one reported for the bulk value (≈0.4 eV[33]) as expected on the basis of scaling of the SO coupling with the number of atoms. In the 2.5 nm–4.5 nm size range, the value of the SO coupling is, therefore, of the order of the 1S–2S gap, ΔE_{1S-2S}, whose magnitude is governed by the QD size, Eq. (2). This leads to a different ordering of the two middle FS bands, $2S_{3/2}$ and $1S_{1/2}$, of the

four excitonic bands as a function of the QD diameter. For mean diameter values, $\bar{D} < \approx 3.2$ nm, the SO splitting of the bands, ΔE_{SO}, is smaller than ΔE_{1S-2S}, which leads to the order $1S_{3/2}$, $1S_{1/2}$, $2S_{3/2}$, $2S_{1/2}$ for the FS bands, as shown in Fig. S1(A) of the supplementary material. When $\bar{D} > 3.2$ nm, we are in the opposite regime, $\Delta E_{SO} > \Delta E_{1S-2S}$, which leads to the order $1S_{3/2}$, $2S_{3/2}$, $1S_{1/2}$, $2S_{1/2}$ [supplementary material, Fig. S1(B)]. Because of the size dispersion, the two middle bands are overlapping and typically cannot be resolved in a UV/VIS absorption spectrum. The two limiting cases can, nevertheless, be identified by the analysis of the 2D maps obtained by 2DES,[36] as we discuss in detail in Sec. III. The four excitonic FS bands are further split by the crystal field and Coulomb interactions. The value of the crystal field splitting, δ_{xf}, is taken to be size independent and equal to 0.025 eV.[33]

There are two kinds of Coulomb interactions, the J (Coulomb) and K (exchange) integrals. Singlet excitons are coupled by both J and K, $J_{mm'}$ and $K_{mm'}$, while triplets are only coupled by the exchange integrals, $K_{mm'}$, where m and m' are exciton labels. The J and K integrals are size-dependent through Eq. (1). In isolated QDs, the Coulomb integrals can have an intraband (within the 1S or 2S bands) or interband (between excitons of the 1S and 2S bands) character. In dimers, they can also have an interdot character, as discussed in Sec. II B. The J and K integrals are computed numerically as described in Ref. 42; see also the supplementary material. In summary, the excitonic Hamiltonian is of the form

$$\hat{H}_{eh}(\mathbf{r},\mathbf{r}') = \hat{H}_e(\mathbf{r}) + \hat{H}_h(\mathbf{r}') + \hat{V}_{Coulomb}(|\mathbf{r}-\mathbf{r}'|) + \hat{V}_{SO} + \delta_{xf} + E_{gap}, \tag{3}$$

where we have dropped the size dependence and δ_{xf} stands for the crystal field splittings. The structure of the 24 × 24 excitonic Hamiltonian matrix for a single dot is given in Fig. 1(b). Upon diagonalization of the Hamiltonian matrix for a single QD, we obtain a set of 24 FS eigenstates per QD.

The transition dipoles to the zero order singlet excitons, m, from the ground state (GS) are computed numerically as a function of the dot diameter, D,

$$\mu^{D}_{GSm} = \int d\mathbf{r}\phi^{h}_{Di}(\mathbf{r})\mathbf{r}\phi^{e}_{Dj}(\mathbf{r}). \tag{4}$$

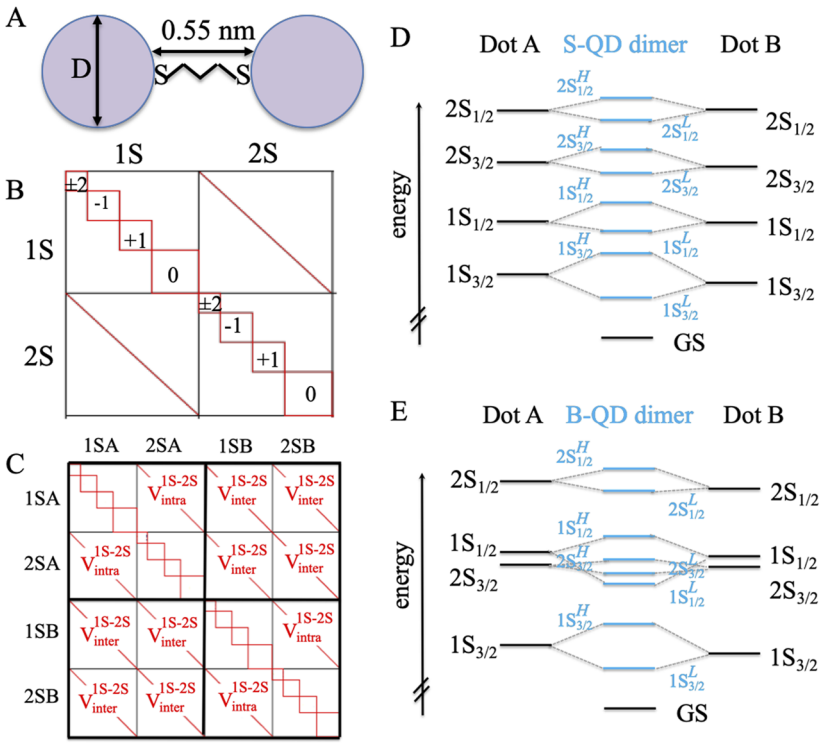

FIG. 1. (a) Schematic representation of the QD dimer. The two QDs are covalently linked by a propanedithiol ligand, which leads to a surface to surface distance of 0.55 nm. The two QDs are drawn from an ensemble of mean diameter $\bar{D}$ = 2.8 nm for the S-QD dimer and 3.5 nm for the B-QD dimer. The ligand length and diameter of the QDs are not on scale. (b) Structure of the fine structure 24 × 24 exciton Hamiltonian matrix for a single QD. Only diagonal and interband Coulomb interactions between excitons of the same nature are retained. The diagonal intraband Coulomb matrix elements are not shown. The off diagonal 1S–2S interband intradot Coulomb coupling is marked as a red line; see the supplementary material for more details. (c) Block structure of the 48 × 48 exciton Hamiltonian matrix for a dimer. A and B are the two dot labels. V^{1S-2S}_{intra} is the intradot interband 1S–2S Coulomb coupling, and V^{1S-2S}_{inter} is the interdot one. (d) Scheme of the energetic order of the eigen-exciton bands for the S-QD dimers. The order of the bands is $1S^{L}_{3/2}$, $1S^{H}_{3/2}$, $1S^{L}_{1/2}$, $2S^{H}_{1/2}$, $2S^{L}_{3/2}$, $1S^{H}_{3/2}$, $2S^{L}_{1/2}$, $2S^{H}_{1/2}$. (e) Scheme of the energetic order of the eigen-exciton bands for the B-QD dimers. The order of the bands is $1S^{L}_{3/2}$, $1S^{H}_{3/2}$, $1S^{L}_{1/2}$, $2S^{L}_{3/2}$, $2S^{H}_{3/2}$, $1S^{H}_{1/2}$, $2S^{L}_{1/2}$, $2S^{H}_{1/2}$.

Upon diagonalization of the matrix Hamiltonian [see Figs. 1(b) and S1(D)], the GS-exciton oscillator strengths are redistributed over the $F = \pm 1$ and $F = 0$ exciton manifolds that are optically allowed. In the size range considered, the transition dipoles to 1S excitons are found to be about two times larger than those to the 2S excitons.[36,42,49]

B. Fine structure levels of the QD dimers

When the distance between two QDs is short enough, they can interact through the Coulomb potential and form stable QD dimers. We report in Sec. III on experimental 2DES measurements on ensembles of QD dimers, obtained by linking with a short propanedithiol ligand two QDs with the same mean size; see Fig. 1(a). Two sizes were considered, $\bar{D}$ = 2.8 nm and $\bar{D}$ = 3.5 nm with 5% dispersion. The case of dimers made of two QDs picked from ensembles of the same mean size is particularly interesting because optimal interdot electronic Coulomb coupling can be achieved.[37] The reason is that each dimer is made of two similar but not quite identical dots. Since the QDs have similar sizes, the effective interdot Coulomb coupling, $V^{eff} = V^{Coul}_{\text{inter}-mm'}/\delta E_{mm'}$, between quasi degenerate eigen-excitons m and m' localized on each of the dots, can be larger than unity: the J and K C integrals [Eqs. (S4) and (S5) of the supplementary material] at the numerator are large because the small interdot distance (a surface to surface distance of 0.55 nm) ensures a good overlap between the hole and electron wave functions, and the energy difference between quasi degenerate eigenstates, $\delta E_{mm'}$, is small.

We model the electronic structure of these QD dimers by drawing 2000 pairs of QDs from a Gaussian ensemble with mean diameter $\bar{D}$ and a size dispersion of 5% and setting the surface to surface distance to the nominal length of the propanedithiol ligand, 0.55 nm. For each dimer, we build an excitonic Hamiltonian where the 24 FS eigenstates on each QD are coupled by interdot Coulomb interactions. We, therefore, only retain local excitons in the basis set used to model the electronic structure of the dimer and neglect the charge transfer (CT) excitons, excitons in which the hole state is localized on one dot and the electron state on the other one. Coulomb interactions between local excitons and CT excitons are at least an order of magnitude smaller than the Coulomb interaction between local excitons.[42] In addition, in dimers built from two QDs drawn from an ensemble of QDs of the same mean size, the energy differences between the states of CT and local exciton bands are larger than those between degenerate bands of local excitons. The effective local-CT exciton coupling is, therefore, very weak. As a result, there is very little mixing between the two groups of excitons in the dimer, and the CT states are essentially dark to optical excitation. The Coulomb coupling between CT excitons is even smaller, two or three orders of magnitude smaller than between CT and local excitons.[42] Hence, CT states do not play any significant role in the ultrafast dynamics that occurs within 100 fs–150 fs after the excitation. In heterodimers for which the sizes of the two QDs can be engineered so that a band of local excitons is overlapping in energy with a band of CT dimer states, the effective coupling between the local and CT states can be larger, but the time scale for the population transfer between the zero order local and CT dimer states remains in the ps time range.[42] Such a coupling between the local (spatially direct) and CT (spatially indirect) excitons has been experimentally observed for GaAs/AlGaAs asymmetric double quantum well samples in which the coupling is phonon assisted.[50,51]

We also neglect the biexciton manifold in the zero order basis set. Assuming that the laser pulse is weak enough to induce only one photon transitions, in the 2DES experimental setup, the biexciton (doubly excited configurations) states can only be accessed by one photon transitions from the exciton (singly excited) states during the third pulse. As discussed in Sec. II D and in Sec. III, the experimental 2D maps only show a very weak signal, barely above the noise limit that could result from contributions due to the excitation of biexcitons. In addition, relaxation to biexcitons typically occurs on a ps time scale via Auger processes.[24,25,52] The biexciton manifold can thus be neglected in the ultrafast time window considered here.

The excitonic Hamiltonian matrix of each dimer is, therefore, a 48 × 48 matrix, as shown in Fig. 1(c), where the diagonal blocks on each dot are those shown in Fig. 1(b). Isolated QDs with $\bar{D}$ = 2.8 nm (called S-QD in what follows) have a level structure that corresponds to Fig. S1(A) ($\Delta E_{\text{S1–S2}} > \Delta E_{\text{SO}}$). The level structure of the QDs with $\bar{D}$ = 3.5 nm (B-QD) corresponds to the level scheme shown in Fig. S1(B) ($\Delta E_{\text{1S–2S}} < \Delta E_{\text{SO}}$). In the dimers, each of the four bands of eigen-excitons on one dot (dot A in Fig. 1) is coupled to the quasi isoenergetic band of the eigen-exciton of the other dot (dot B) by the interdot Coulomb coupling. Upon diagonalization of the Hamiltonian matrix for the dimers shown in Fig. 1(c), we, therefore, obtain two dimer eigen-exciton bands for each band of local excitons of the isolated dots, a low one and a high one, separated in energy by about twice the strength of the Coulomb interdot coupling. In total, therefore, there are eight dimer eigen-exciton bands that we label $1S^L_{3/2}$, $1S^H_{3/2}$, $2S^L_{3/2}$, $2S^H_{3/2}$, $1S^L_{1/2}$, $1S^H_{1/2}$, $2S^L_{1/2}$, $2S^H_{1/2}$.

The splittings between the excitonic bands due to Coulomb interdot interactions depend on both the magnitude of the interdot Coulomb matrix elements and the spacings between two quasi degenerate eigen-excitons on each QD in the dimer. The interdot Coulomb coupling, $V^{Coul}_{\text{inter}-mm'}$, where m and m' stand for the index of an eigen-exciton of a single QD, is the largest between excitons with the same hole function on each dot, and it is larger between excitons of the 1S type than for those of the 2S type. The reason is that the 1S hole wave functions are more delocalized outside the classical well than the 2S ones and do not have a node.[38,42] The interdot Coulomb integrals have been computed numerically as described in Ref. 42 (see also the supplementary material) for an ensemble of 2000 dimers. The histograms of the interdot Coulomb coupling strengths are approximately Gaussian. We observe three ranges of mean coupling values, depending on the nature of the pair of states m and m' involved. The mean value of the interdot coupling between states belonging to the 1S band [$V^{\text{1S–1S}}_{\text{inter}}$ in Fig. 1(c)] is of the order of 45 meV for S-QD dimers and 35 meV for B-QD ones, while for the 2S bands, the value of $V^{\text{2S–2S}}_{\text{inter}}$ is much smaller, of the order of 5 meV for the S-QD dimers and 2 meV for B-QD ones. The interdot interband coupling, $V^{\text{1S–2S}}_{\text{inter}}$, has an intermediate mean value of 15 meV for the S-QD dimers and 10 meV for B-QD ones. In summary, the interdot Coulomb integrals are on the average smaller than the 1S–2S gap, $\Delta E_{\text{1S–2S}}$, and also smaller than the SO coupling, ΔE_{SO}. The dimer level structures of excitonic bands are shown schematically in Figs. 1(d) and 1(e) for the two sizes investigated.

The distribution of the spacings, $\delta E_{mm'}$, between two eigen-excitons of isolated dots A (m) and B (m') in the dimer, exhibits two peaks, depending on whether m and m' belong to the same band on each exciton or not. The distribution of spacings has a mean value of the order of 60 meV for the quasi degenerate states belonging to the 1S band on each dot and of 120 meV for the 2S band. In both bands, there is a group of very small spacings due to accidental quasi degeneracies between eigen-excitons localized on each dots. The mean value of $\delta E_{mm'}$ is of the order of 480 meV for 1S–2S spacings. The distribution of spacings of the 2S states is broader than that of the 1S ones because 2S states are more sensitive to the size fluctuations.

The effective interdot coupling strengths, $V^{eff}_{mm'} = V^{Coul}_{\text{inter}-mm'}/\delta E_{mm'}$, govern the value of the splitting of the excitonic bands in the dimer. In the dimers that we investigate here, the effective coupling is rather large, >1, because the dot mean size is small (<4.5 nm), the propanedithiol ligand has a short length of 0.55 nm, and the size dispersion is low, which leads to a narrow width of the spacing distribution. The distribution of the $V^{Coul}_{\text{inter}-mm'}$ values is shown in Fig. 2 for the three pairs of excitons representative of the 1S–1S, 2S–2S, and 1S–2S coupling for S-QD dimers. The largest effective coupling strengths are found for the pairs of excitons that belong to the 1S band on each dot [Fig. 2(a)], with a mean effective coupling strength value of 6.8, while it is 0.4 for states belonging to the 2S band in each dot [Fig. 2(b)]. These high values can be understood from the accidental quasi degeneracies between eigen-excitons on each dot. The effective coupling between states belonging to different bands on the two dots is very small, of the order of 0.04 [Fig. 2(c)]. In the case of the B-QD dimers, the mean values of the Coulomb couplings are systematically smaller because the hole and electron wave functions are more confined inside the classical well when the size is larger. However, the two sizes considered here are very close, so the differences in coupling are less than a factor of 2 compared to the S-QD's. The mean values of the spacings are also smaller, which leads overall to the same order of magnitude and trends for effective interdot coupling strengths for the B-QD dimers.

The high values of V^{eff} between states of the 1S band ensure a significant delocalization of the eigenstates of dimers on the two dots. We quantify the interdot electronic delocalization of the eigenstates of the dimer, label k, on the basis of the parameter M_k defined as

$$M_k = 1/\left[(W_{Ak})^2 + (1 - W_{Ak})^2\right], \tag{5}$$

where W_{Ak} is the weight of the dimer eigenstate k on the states of dot A, $W_{Ak} = \sum_{m=1}^{24} |c_{mk}|^2$, with c_{mk} being the amplitudes of the dimer eigenstate k on the eigen-excitons of dot A. M_k is equal to 2 for a dimer eigen-exciton equally delocalized on dots A and B and to 1 for an eigen-exciton fully localized either on dot A or on dot B.

We show in Fig. 3 the mean value of the coefficient $\langle M_k \rangle$ computed over the ensemble of 2000 dimers for the S-QD dimers [panel (a)] and the B-QD dimers [panel (b)]. In both panels, the dimer eigen-excitons are ordered by increasing energy. For the S-QD dimers [panel (a)], one can see that for the first 24 eigenstates, which are those that are mainly localized on the 1S bands [$1S_{3/2}$ and $1S_{1/2}$; see Fig. 1(c) on each dot], the mean value of $\langle M_k \rangle$ is about 1.6. It is much smaller (about 1) for eigen-excitons of the two 2S exciton bands, $2S_{3/2}$ and $2S_{1/2}$, which are poorly mixed by interdot Coulomb interactions. For the B-QD dimers [panel (b)], we see that the lowest dimer eigenstates, up to state 15, also have a $\langle M_k \rangle$ value of ≈1.6. They have weights on the $1S_{3/2}$ states of each dot and are well delocalized over the two dots. Then, from state 17 to state 40, the dimer eigenstates have weights on the bands $2S_{3/2}$ and $1S_{1/2}$ of dots A and B. These two bands overlap and are less effectively mixed by the Coulomb interactions, which leads to lower $\langle M_k \rangle$ values. States above state 40 are localized on $2S_{1/2}$ states and have a $\langle M_k \rangle$ value barely larger than 1. Because of the mixing induced by the interdot coupling, the oscillator strengths of the eigen-excitons of each dot [Eq. (4)] are redistributed over the eigen-excitons of the dimer.

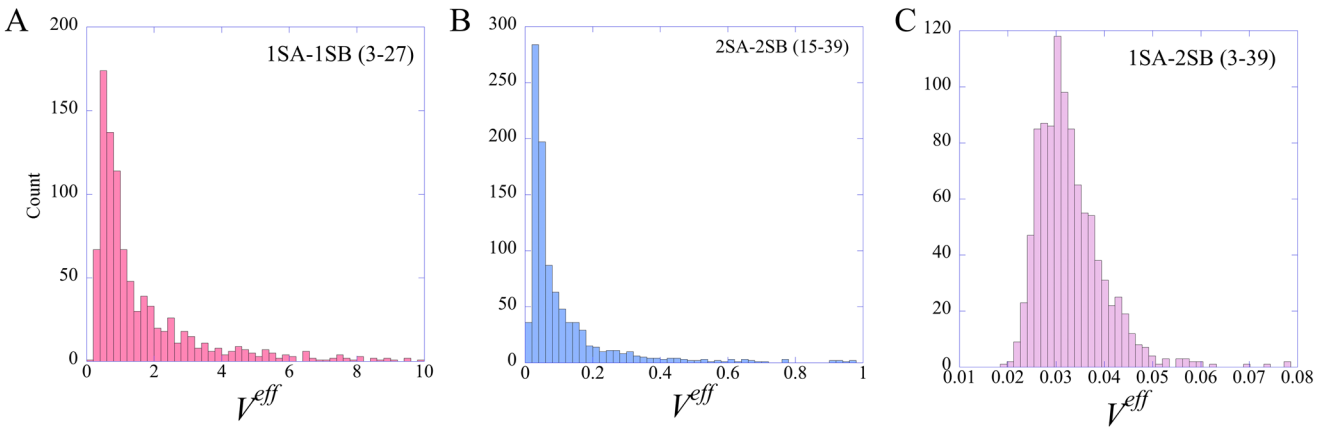

FIG. 2. Histograms of the effective interdot coupling, V^{eff}, computed for an ensemble of 2000 S-QD dimers drawn from ensembles with $\bar{D}$ = 2.8 nm. (a) V^{eff} between two excitons that belong to the 1S band on each dot, m = 3, m' = 27. (b) V^{eff} between two excitons belonging to the 2S band (m = 15, m' = 39). (c) V^{eff} between one exciton belonging to a 1S state on QD_A(m = 3) and a 2S state on QD_B (m' = 39). Note that for panels (a) and (b), the small group of very high values of V^{eff} > 10 and >1, respectively, due to the accidental quasi degeneracies between eigen-excitons on each dot is not shown.

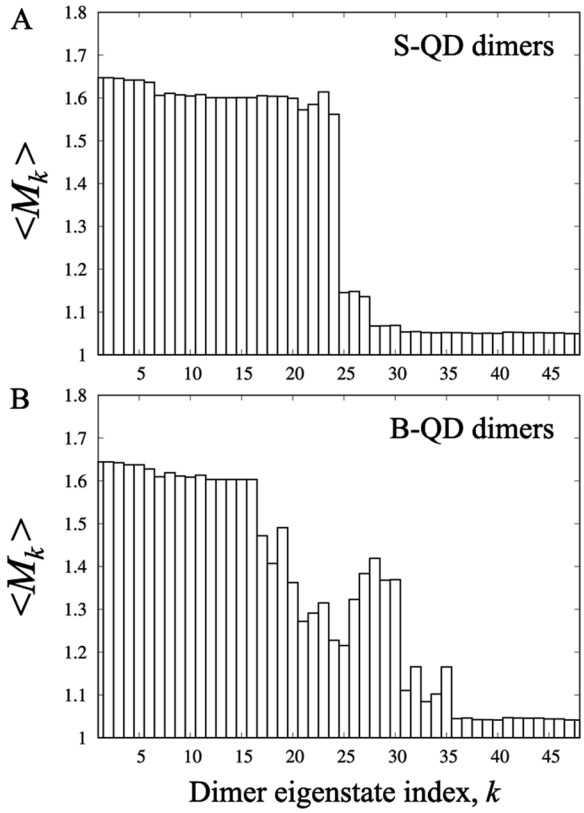

FIG. 3. Mean value of the interdot delocalization parameter, $\langle M_k \rangle$ [Eq. (5)] of the dimer eigenstates, k, computed over an ensemble of 2000 S-QD (small QD) dimers [panel (a)] and B-QD (big QD) dimers [panel (b)].

C. Liouvillian dynamics of the ensemble of QDs

We compute the response of an ensemble of non-interacting dimers to the sequence of three fs pulses as used in the 2DES setup, using the Liouvillian ensemble approach described in Ref. 38. We show that this approach is particularly well-suited when the polarization resulting from the interaction of the dimers with three laser pulses as used in 2DES is approximated by third order perturbation theory in the framework of the impulsive limit and the rotating wave approximation. The sequence of the three laser pulses and the three time intervals that they define is shown schematically in Scheme 1. τ is the time interval between the first and second pulses, T is the time interval between the second and third pulses, and the time t is the time interval between the third pulse and the emission back to the ground state.

The total electric field at position $\mathbf{r}$ is given by

$$\mathcal{E}_{tot}(\mathbf{r},t) = \sum_{n=1}^{3} \mathcal{E}_n(\mathbf{r},t) + P_{ens}(\mathbf{r},t), \tag{6}$$

where $\mathcal{E}_n(\mathbf{r}, t)$ is the time profile of the electric field of nth pulse in the sequence, which has a finite duration represented by a Gaussian envelope of width σ_n,

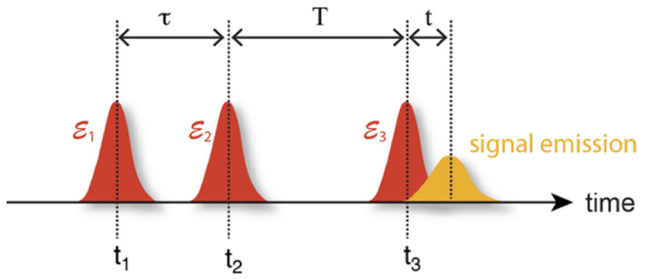

SCHEME 1. Pulse sequence in a typical 2DES experiment and time delays' definition.

$$\begin{aligned}\mathcal{E}_n(\mathbf{r},t) &= \mathcal{E}_n \exp\left(-\frac{(t-t_n)^2}{2\sigma_n^2}\right)\cos(\omega_n t - \mathbf{k}_n\cdot\mathbf{r}) \\ &= \mathcal{E}_n \exp\left(-\frac{(t-t_n)^2}{2\sigma_n^2}\right)(\exp(i(\omega_n t - \mathbf{k}_n\cdot\mathbf{r})) \\ &\quad + \exp(-i(\omega_n t - \mathbf{k}_n\cdot\mathbf{r}))),\end{aligned} \tag{7}$$

where $\mathcal{E}_n = |\mathcal{E}_n|\hat{\mathbf{e}}_n$, $\hat{\mathbf{e}}_n$ is the polarization of the electric field, $|\mathcal{E}_n|$ is its strength, ω_n is its carrier frequency, and $\mathbf{k}_n$ is its wave vector.

$P_{ens}(\mathbf{r}, t)$ is the total polarization of the ensemble of M dimers at position $\mathbf{r}$. For an ensemble of non-interacting dimers, it is the sum of the polarization of each dimer,

$$\mathbf{P}_{ens}(\mathbf{r},t) = \sum_{\alpha}^{M} \mathbf{P}_\alpha(\mathbf{r}-\mathbf{r}_\alpha, t), \tag{8}$$

where α is the index of a dimer and $\mathbf{P}_\alpha(\mathbf{r} - \mathbf{r}_\alpha, t)$ is the polarization at $\mathbf{r}$ due to the dimer α at the position $\mathbf{r}_\alpha$. $\mathbf{P}_\alpha(\mathbf{r} - \mathbf{r}_\alpha, t)$ can then be decomposed into the directional components given by the phase matching directions.[43]

In the specific case of 2DES using weak laser pulses, two specific phase matching directions are typically accessed, referred to as "rephasing" and "non-rephasing,"[46,53] and therefore, only these two spatial components will be considered in the following.

The polarization of each dimer, $\mathbf{P}_\alpha(t)$, (where from now on we do not explicitly denote the $\mathbf{r}$ dependence) is given by

$$\mathbf{P}_\alpha(t) = \mathrm{Tr}[\hat{\mu}\hat{\rho}_\alpha(\tau,T,t)], \tag{9}$$

where $\hat{\mu}$ is the dipole operator and $\hat{\rho}_\alpha(\tau, T, t)$ is the density matrix of the dimer α that results from its interaction with the three pulses,

$$\hat{\rho}_\alpha(\tau,T,t) = \sum_{m,n}^{N} \rho_\alpha^{mn}(\tau,T,t)|m\rangle\langle n| = \sum_{m,n}^{N} \rho_\alpha^{mn}(\tau,T,t)\hat{E}_{mn}, \tag{10}$$

where $\hat{E}_{mn} \equiv |m\rangle\langle n|$. The operators, $\hat{E}_{mn}$, can be represented in the basis of the eigen-excitons of the dimer by the $N \times N$ Gelfand matrices[54] that have entries equal to 0 everywhere except at row m and column n where the entry is equal to 1. The Gelfand matrices and the operators, $\hat{E}_{mn}$, satisfy the commutation relation of the Lie algebra U(N),

$$\left[\hat{E}_{mn}, \hat{E}_{kl}\right] = \hat{E}_{ml}\delta_{nk} - \hat{E}_{kn}\delta_{lm}. \tag{11}$$

The N diagonal elements of the density matrix, $\rho_\alpha^{nn}(\tau,T,t)$, correspond to the populations in eigen-excitons, $n = 1, \ldots, N$, and the off diagonal elements, $\rho_\alpha^{mn}(\tau,T,t)$, are the $N(N-1)$ complex amplitudes of the electronic coherences, $\rho_\alpha^{mn}(\tau,T,t) = (\rho_\alpha^{nm}(\tau,T,t))^*$. As detailed in Sec. II B, each dimer in the ensemble is made of two dots of a slightly different size and, therefore, has a slightly different set of eigen-excitons. When the dimer interacts with the electric field, the eigenstates are coupled by the dipole interaction, and the excitonic Hamiltonian is off diagonal and has a time-dependent part,

$$\begin{aligned}\hat{H}_\alpha &= \sum_{m,n} H_\alpha^{mn}(t)\,\hat{E}_{mn} \\ &= \sum_{n=1}^{N} E_\alpha^n \hat{E}_{nn} - \sum_{n=1}^{3} \boldsymbol{\mathcal{E}}_n(\mathbf{r},t)\cdot \sum_{m,n\neq m}^{N} \mu_\alpha^{mn}\hat{E}_{mn},\end{aligned} \tag{12}$$

where μ_α^{mn} is the transition dipole between the eigen-excitons m and n of the dimer α and $\sum_{n=1}^{3}\boldsymbol{\mathcal{E}}_n(\mathbf{r},t)$ is the sequence of the three pulses given by Eq. (7).

The total Hamiltonian, Eq. (12), the density matrix Eq. (10), and the commutator [Eq. (11)] are linear combinations of the N^2 operators, $\hat{E}_{mn}$. In that case, the density matrix of the N state system, and, in general, any observable of the system, can be written as a linear combination of the N^2, $N \times N$, Gelfand matrices that represent the $\hat{E}_{mn}$ operators.[55] The fact that the Hamiltonian, $\hat{H}_\alpha$, is a linear combination of the operators, $\hat{E}_{mn}$, and the closure property [Eq. (11)] implies that the Heisenberg equation of motion of the $\hat{E}_{mn}$ is also closed, and it is given by

$$\begin{aligned}i\hbar\frac{\partial \hat{E}_{mn}}{\partial t} &= \left[\hat{E}_{mn},\hat{H}_\alpha\right] = \sum_{k,l}^{N} H_\alpha^{kl}\left[\hat{E}_{mn},\hat{E}_{kl}\right] \\ &= \sum_{l} H_\alpha^{nl}\hat{E}_{ml} - \sum_{k} H_\alpha^{kn}\hat{E}_{km}.\end{aligned} \tag{13}$$

For the coherences, $\rho_\alpha^{mn}(t)$, taking an average of Eq. (13) over the density matrix of the dimer, one gets a closed set of equations of motion,

$$i\hbar\frac{\partial \rho_\alpha^{mn}(t)}{\partial t} = i\hbar\frac{\partial \langle E^{nm}\rangle_\alpha}{\partial t} = \sum_{l}^{N} H_\alpha^{ml}(t)\langle E_{nl}\rangle_\alpha - \sum_{k}^{N} H_\alpha^{kn}(t)\langle E_{km}\rangle_\alpha, \tag{14}$$

$$i\hbar\frac{\partial \rho_\alpha^{mn}(t)}{\partial t} = \sum_{l}^{N} H_\alpha^{ml}(t)\rho_\alpha^{ln}(t) - \sum_{k}^{N} H_\alpha^{kn}(t)\rho_\alpha^{mk}(t). \tag{15}$$

There is a separate set of the N^2 equations of motion for each size α.

It is possible to write Eq. (15) in terms of a Liouvillian matrix, listing the indices of the N^2 elements of the density matrix in lexicographic order,

$$i\hbar\frac{\partial \rho_\alpha^{mn}(t)}{\partial t} = \sum_{kl}^{N} L_{mn,kl}\rho_\alpha^{kl}(t). \tag{16}$$

The density matrix of the ensemble of dimers is a mixture: $\hat{\rho} = \sum_\alpha^M p_\alpha\hat{\rho}_\alpha$, and the electronic coherence of the ensemble is given by its average over the size distribution,

$$\rho^{mn}(t) = \sum_{\alpha}^{M} p_\alpha \rho_\alpha^{mn}(t). \tag{17}$$

Determining the density matrix for the ensemble requires solving the dynamics using Eq. (16) for each dimer size and then performing the average (17).

For non-interacting dimers, the average Hamiltonian of the ensemble, $\hat{H}$, is diagonal in the index α,

$$\begin{aligned}\hat{H} &= \sum_{\alpha}^{M}|\alpha\rangle\hat{H}_\alpha\langle\alpha| = \sum_{\alpha}^{M}|\alpha\rangle\left(\sum_{m,n}^{N} H_\alpha^{mn}\hat{E}_{mn}\right)\langle\alpha| \\ &= \sum_{m,n}^{N}\left(\sum_{\alpha}^{M}|\alpha\rangle H_\alpha^{mn}\langle\alpha|\right)\hat{E}_{mn} \\ &= \sum_{m,n}^{N} H^{mn}\hat{E}_{mn}.\end{aligned} \tag{18}$$

As pointed out above, when no pulse is acting, the Hamiltonian of each dimer, H_α, is diagonal in the eigen-exciton basis, and therefore, the averaged Hamiltonian of the ensemble is equally diagonal. In the absence of the laser pulses, one can, therefore, analytically determine the density matrix for the ensemble. See Eq. (23). Not so when the lasers are on. The matrix elements of the total Hamiltonian of the ensemble then take the form

$$\begin{aligned}H^{mn} &= \sum H_\alpha^{mn} = \sum_\alpha E_\alpha^n\delta_{mn} - \boldsymbol{\mathcal{E}}(t)\cdot\sum_\alpha \mu_\alpha^{mn}, \\ H^{mn} &= H_0^{mn} - \boldsymbol{\mathcal{E}}(t)\cdot\bar{\mu}_{mn} = \bar{\epsilon}_m\delta_{mn} - \boldsymbol{\mathcal{E}}(t)\cdot\bar{\mu}_{mn},\end{aligned} \tag{19}$$

where E_α^n are the energies of the stationary states of the dimer in the absence of interaction with the pulse, μ_α^{nm} are the transition dipole matrix elements in the basis of the eigen-exciton of the dimer, and $\boldsymbol{\mathcal{E}}(t)$ is the time profile of the electrical field of the laser pulses [Eq. (6)]. $\bar{\epsilon}_n$ and $\bar{\mu}_{nm}$ are the average values of the stationary energies and the transition dipoles over the ensemble of dimers.

Unlike the case of a single dimer [Eq. (14)], the equations of motion of the average coherences, $\rho^{mn}(t)$, are not closed. This implies that for computing the polarization of the ensemble [Eq. (8)], one has to solve the equations of motion of the coherences for each dimer separately and compute its polarization P_α [Eq. (9)].

We have shown in Ref. 38 that one can define an approximate ensemble density matrix, $\hat{\rho}_c(t)$, that is a very good approximation to the density matrix of the ensemble, $\hat{\rho}(t)$, but whose equations of motion remain closed when propagated by the Hamiltonian $\hat{H}$ [Eq. (19)] of the ensemble of dimers,

$$\hat{\rho}_c(t) = \sum_{kl}\rho_c^{kl}(t)\hat{E}_{kl}, \tag{20}$$

and

$$i\hbar\frac{\partial\hat{\rho}_c}{\partial t} = \left[\hat{H},\hat{\rho}_c\right], \tag{21}$$

$$i\hbar\frac{\partial\rho_c^{mn}}{\partial t} = \sum_{k}^{N} H_{mk}\rho_c^{kn} - \sum_{l}^{N} H_{ln}\rho_c^{ml}. \tag{22}$$

When no pulse is present, in a time interval $(t-t_0)$, the Hamiltonian, Eq. (19), is diagonal for each dimer, and the average coherence at time t is given by

$$\begin{aligned}\boldsymbol{\rho}^{mn}(t) &= \textstyle\sum_{\boldsymbol{\alpha}} p_{\boldsymbol{\alpha}}\boldsymbol{\rho}_{\boldsymbol{\alpha}}^{mn}(t) \\ &= \textstyle\sum_{\boldsymbol{\alpha}} p_{\boldsymbol{\alpha}}\exp\left(-i\left(H_{\boldsymbol{\alpha}}^{mm} - H_{\boldsymbol{\alpha}}^{nn}\right)(t-t_0)\right)\boldsymbol{\rho}_{\boldsymbol{\alpha}}^{mn}(t_0).\end{aligned} \tag{23}$$

We showed in Ref. 38 that when no pulse is present, $\rho^{mn}(t)$ can be well approximated in a closed form,

$$\rho^{mn}(t) = \sum_\alpha p_\alpha \exp\left(-i\left(H_\alpha^{mm} - H_\alpha^{nn}\right)(t-t_0)\right)\rho_\alpha^{mn}(t_0) \approx \left(\sum_\alpha p_\alpha \exp\left(-i\left(H_\alpha^{mm} - H_\alpha^{nn}\right)(t-t_0)\right)\right)\rho_c^{mn}(t_0), \quad (24)$$

where $\rho_c^{mn}(t)$ is defined by Eqs. (20)–(22). The time evolution in the second line of Eq. (24) can be approximated using the cumulant expansion[38] for an average over the size distribution of the frequency differences $\delta\Omega = (H_\alpha^{mm} - H_\alpha^{nn})$,

$$\ln\langle\exp(it\delta\Omega)\rangle = \mu it - \left(\frac{\sigma^2}{2}\right)t^2 - i\frac{\kappa_3}{3!}t^3 + \frac{\kappa_4}{4!}t^4 + \cdots, \quad (25)$$

where μ is the mean, σ^2 is the variance, and κ_3 and κ_4 are the third and the fourth cumulants of $\delta\Omega$. Using the first three cumulants in Eq. (25), we get

$$\rho^{mn}(t) \approx \rho_{ens}^{mn}(t) = \exp\left(-i\tilde{\omega}_{mn}(t-t_0) - i\frac{\kappa_3}{6}(t-t_0)^3\right) \times \exp\left(-\sigma_{mn}^2\frac{(t-t_0)^2}{2}\right)\rho_c^{mn}(t_0). \quad (26)$$

In Eq. (26), the mean coherence period and its variance are given by

$$\tilde{\omega}_{mn} = \sum_\alpha p_\alpha\left(H_\alpha^{mm} - H_\alpha^{nn}\right) = \tilde{e}_m - \tilde{e}_n, \quad (27)$$

$$\sigma_{mn}^2 = \sum_\alpha p_\alpha\left(H_\alpha^{mn} - H_\alpha^{nn}\right)^2 - \tilde{\omega}_{mn}^2. \quad (28)$$

The expressions of κ_3 and κ_4 are given in the supplementary material. Using Eq. (26) allows describing the coherent dynamics of the ensemble when no pulse is present by a single time propagation, using Hamiltonian H [Eq. (18)]. It only involves stationary properties of the eigen-excitons of each dimer of the ensemble. It requires computing the eigen-excitons of each dimer as described in Sec. II B and the coefficients of the cumulant expansion, Eq. (25), for an ensemble of size dispersed dimers. We have shown in Ref. 38 that Eq. (26) provides an excellent approximation to the exact dynamics [Eq. (17)], which requires to propagate the coherences of each dimer separately and then average over the ensemble. Equation (26) is valid for any Hermitian operator acting on the ensemble. We are using it below to compute the 2D maps in the impulsive limit. In this limit, Eq. (26) provides an efficient route for computing the 2D maps for an ensemble of QDs without having to compute the dynamics of each dimer interacting with the sequence of three laser pulses, which becomes rapidly prohibitive because of the large number of dimers that need to be included in the ensemble. Equation (26) includes the inhomogeneous dephasing of the electronic coherences due to the finite size dispersion of the QDs through the cumulant expansion, Eq. (25). The shifts of the mean induced by the third cumulant remain very small and are neglected; see Sec. 2 of the supplementary material and discussion in Sec. II D. In the solid state device of size dispersed QDs studied here, the widths due to the inhomogeneous broadening induced by the 5% size dispersion (≈300 cm^{-1}–1000 cm^{-1}, see Table S1) are larger than thermal broadening at room temperature and also larger than or commensurate with reported homogeneous broadening due to the coupling between electronic states and phonon modes, surface traps, and carrier relaxation for similar QDs.[20,23,28,56–59] The observed dephasing times during the first 150 fs–200 fs of the dynamics are consistent with being dominated by the 5% size dispersion.

D. Computation of the maps in the impulsive limit for weak pulses

In the limit of weak pulses and in the impulsive limit for which the duration of the pulse is described by a delta function $\delta(t)$ in Eq. (7), one assumes a one photon process occurring at the maximum of the pulse envelope of the three pulses, t_1, t_2, t_3 in Scheme 1. On can then write the density matrix $\hat{\rho}$ to third order in time-dependent perturbation theory and then use standard nonlinear response function theory[43–45] to calculate the response function, $S_{ens}^{(3)}(\tau, T, t)$, and the associated polarization. The emitted signal by the ensemble is given by

$$\boldsymbol{\mathcal{E}}_{emi}(\tau, T, t) = i\mathbf{P}_{ens}(t) \propto i\boldsymbol{\mathcal{E}}_3(\tau+T)\boldsymbol{\mathcal{E}}_2(\tau)\boldsymbol{\mathcal{E}}_1(0)S_{ens}^{(3)}(\tau, T, t).$$

In standard nonlinear response theory, the response function is given by the expectation of the dipole moment computed for the density matrix to third order,

$$S_{ens}^{(3)}(\tau, T, t) = \left(\frac{-i}{\hbar}\right)^3 \mathrm{Tr}(\hat{\mu}_4(t+T+\tau)[\hat{\mu}_3(\tau+T),[\hat{\mu}_2(\tau),[\hat{\mu}_1(0),\hat{\rho}(0)]]]). \quad (29)$$

We compute the third order response using nested commutators as shown in Eq. (29). The time evolution is given by the Hamiltonian $\hat{H}$ of the ensemble [Eqs. (18) and (19)], and we approximate the density matrix of the ensemble as $\hat{\rho}_c$, see Eq. (20), whose propagation in time is determined by the ensemble Hamiltonian. Between the pulses, the ensemble evolves according to the stationary Hamiltonian of the ensemble, H_0, and the time evolution of the elements, $\rho_{ens}^{mn}(t)$, of the approximate density matrix of the ensemble is given by Eq. (26).

The third order response, $S_{ens}^{(3)}(\tau, T, t)$, Eq. (29), corresponds to a large number of Liouvillian paths that are defined by the commutators $[\hat{\mu}, \hat{\rho}_c]$ of Eq. (29). For computing the 2D maps, we only retain the subset that contributes to the signal emitted in specific phase matching directions.[43–46,53] Conventionally, the relevant diagrams contributing to the third order signal can be classified as ground state bleaching (GSB) or stimulated emission (SE), which describe contributions where during the population time, T, the system is evolving in the ground or in an excited state, respectively. A third kind of diagrams describing Excited State Absorption (ESA) could also contribute to the maps. These diagrams are due to excitations to doubly excited configuration states (biexcitons or two exciton states), which can be accessed by one photon transitions from mono-exciton states during the third pulse. ESA pathways lead to negative contributions to the signal in the 2D maps. However, the experimental 2D maps (see discussion on Fig. 6 in Sec. III) only exhibit a small negative signal. The fact that the ESA contributions are small is due to the small number of population that is transferred to the doubly excited states during the interaction with the third pulse (we estimate 1% transfer, compared to 10% for the single excited states) and the fact that both the mono and biexciton states have large inhomogeneous

widths. Indeed, the most intense (weak) negative contributions in the 2D maps shown in Fig. 6 can be accounted for by the model that does not include the biexciton manifold. We, therefore, did not include ESA diagrams in the modeling of the maps. These different diagrams can be further classified into non-oscillating paths, represented by Feynman diagrams where the system reaches a pure state after the first two interactions and oscillating contributions described by Feynman diagrams where, after the first two interactions, the system is in a coherent superposition of states.[44,46,60,61]

In building the maps, it is assumed that the dimers in the ensemble that contribute in a given phase matching direction follow the same set of Liouvillian paths that are given by the allowed double-sided Feynman diagrams. Since the number M of dimers in the ensemble has to be very large, the properties of the distribution of levels in each subset of dimers can be described by the cumulants given by Eqs. (27) and (28).

In the experiments reported below, the laser bandwidth is such that one photon transitions are allowed to all or a subset of fine structure excitonic bands shown in Figs. 1(d) and 1(e).

For a pair of excitons m, n and the ground state (GS), we have eight Liouville paths for the rephasing "photon echo" direction and eight Liouville paths for the non-rephasing one. Their explicit expressions are given in the supplementary material, Eqs. (S6) and (S7).

For the short times investigated here, only the inhomogeneous broadening due to the size dispersion contributes to the response. We neglect in Eqs. (S6) and (S7) the contribution of the third and fourth cumulants in Eq. (25). As explained above, to compute the eigen-energies of the dimers of the ensemble, we draw the QD size from a Gaussian distribution with a given mean diameter, $\bar{D}$, for each dot and a size dispersion of 5%, compute the single particle energies for the electron (1S), hole (1S), and hole (2S) for the size of each dot of the dimer, build the electronic Hamiltonian for the dimer for this given pair of sizes of the two QDs, and diagonalize it. We characterize the eigen-energy distributions by a cumulant expansion [Eq. (26)]. The values of the first four cumulants for the 48 excitons are reported in Table S1 of the supplementary material for the S-QD dimers as well as histograms of the eigen-energies distributions for selected excitons (Fig. S2). We find that the distributions of the transition frequencies from the GS to the excitons are well described by the first two cumulants, which leads to Gaussian distributions. The skewness, which gives the asymmetry of the eigen-energy distributions with respect to the variance, is on the average 10%–20% with higher values for dimer states of the S2 band than for the S1 ones. The kurtosis, which characterizes the deviation of the tails of the distribution with respect to a Gaussian, is of the order of 5%–10% of the variance with the same trend that the kurtosis is larger for dimer states of the S2 band than of the S1 one. This is due to the fact that the distribution in energy of the single particle hole S2 states is wider than those of the hole S1 and electron states.[38,42] The slight asymmetry in the eigen-energy distribution of the dimers can be understood from the fact that the eigen-energies of the one particle states in each QD scale approximately as $1/D^2$ (D is the diameter).[2] The resulting asymmetry due to the Jacobian in $E^{-1.5}$ of the distributions of the energies of the single particle states is small because of the small value of the mean diameter of the QD considered here ($\bar{D}$ = 2.8 nm and 3.5 nm) and the narrow size distributions. As a result, the distributions of the eigen-energies of the ensemble of dimers remain Gaussian in a very good approximation as can be judged for the fits to Gaussian distributions shown in Fig. S2 for selected eigenstates.

The 2D frequency maps are obtained by Fourier transforming the responses along τ and t for specific values of T,

$$S^{(3)}_{ens-mn}(\omega_\tau, T, \omega_t) = i \int_0^{t_f} dt \int_0^{\tau_f} d\tau \, S^{(3)}_{ens-mn}(\tau, T, t) \times \exp(i\omega_\tau \tau) \exp(-i\omega_t t). \quad (30)$$

As can be seen from Eqs. (S6) and (S7), the abscissa and ordinate of the map correspond to the transition frequencies from the GS to excitons, inhomogeneously broadened by a Gaussian of widths σ_{0m} and σ_{0n}, respectively, that depends on the size dispersion of the QDs; see Table S1 of the supplementary material for the computed values of the 24 GS-exciton transition frequencies in a single QD and 48 GS-exciton ones in the dimers.

Among the eight identified relevant paths, only two exhibit a periodic time-dependence with respect to T, which corresponds to the transition frequency, $\bar{\omega}_{mn}$, between the excitons m and n. These two periodically oscillating contributions are the signature of coherences between excitons. We call these coherences inter-exciton coherences in what follows. In the rephasing direction [supplementary material, Eq. (S6)], they appear at the addresses $(\bar{\omega}_{0m}, \bar{\omega}_{0n})$ and $(\bar{\omega}_{0n}, \bar{\omega}_{0m})$ on the map and dephase in time as Gaussians, with dephasing times given by $1/\sigma_{mn}$, the σ_{mn} values being obtained using Eq. (28) above. Two non-oscillating GSB paths also contribute to these addresses. The two other GSB paths and the two SE paths contribute to the diagonal at the addresses $(\bar{\omega}_{0m}, \bar{\omega}_{0m})$ and $(\bar{\omega}_{0n}, \bar{\omega}_{0n})$. In the non-rephasing direction [supplementary material, Eq. (S7)], the oscillating paths corresponding to the inter-exciton coherences appear on the diagonal at the addresses $(\bar{\omega}_{0m}, \bar{\omega}_{0m})$ and $(\bar{\omega}_{0n}, \bar{\omega}_{0n})$, while the other contributions are identical.

The 2D maps are computed by summing these eight paths for each pair of the excited states [$N(N-1)/2$], where $N = 24$ for a single QD and 48 for a dimer. Each transition is characterized by a mean transition frequency and a width given by Eqs. (27) and (28),

$$S^{(3)}_{ens}(\omega_\tau, T, \omega_t) = \sum_{m=1}^{N} \sum_{n>m}^{N} S^{(3)}_{ens-mn}(\omega_\tau, T, \omega_t). \quad (31)$$

The double Fourier transform in Eq. (30) is computed numerically because of its causal character resulting from the time ordering of the pulses. The Fourier transforms of the Gaussian decays for t and $\tau \geq 0$ have both a real and an imaginary part that lead to small negative contributions in the computed maps that are in agreement with the ones present in the experimental ones (see Fig. 6 below). We also report in the supplementary material (Figs. S3 and S4) maps computed by adding a homogeneous width of 0.01 eV to each exciton, which leads to an exponential decay factor in Eq. (26). In that case, the real part of the Fourier transform exhibits a Voigt profile.

For a given amount of size dispersion, the values of the mean widths, $\bar{\sigma}_{mn}$, depend on the nature of the excitons involved in the transition. The inhomogeneous widths of the transition from the GS, $\bar{\sigma}_{0m}$, are wider for excitons that involve a hole of type 2S than those of type 1S because, as explained in Sec. II B, the energies of the 2S excitons are more sensitive to the variation in size. The

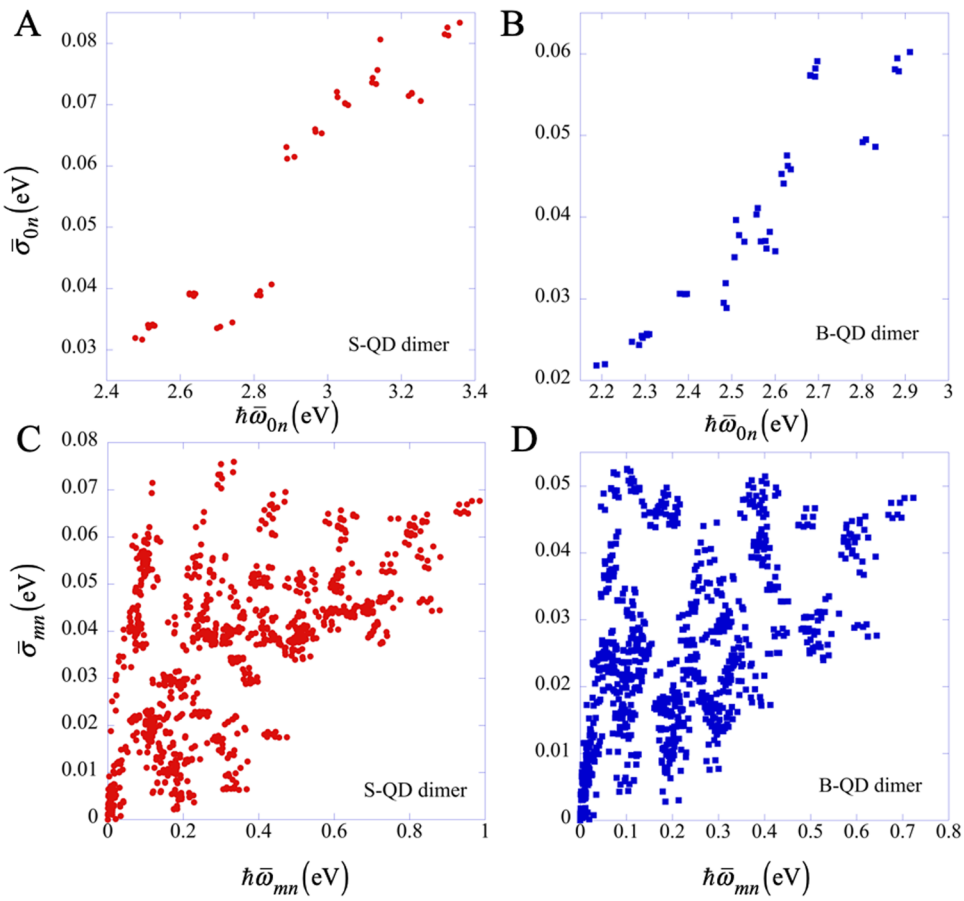

FIG. 4. Dephasing widths ($\bar{\sigma}_{mn}$) between mean transition energies ($\hbar\bar{\omega}_{mn}$) computed for an ensemble of 2000 S-QD dimers [panels (a) and (c), $\bar{D}$ = 2.8 nm] and B-QD dimers [panels (b) and (d), $\bar{D}$ = 3.5 nm]. The size dispersion is 5%. (a) Transition GS-exciton for S-QD dimers. (b) Transition GS-exciton for B-QD dimers. (c) Inter-exciton transitions for S-QD dimers. (d) Exciton–exciton transitions for B-QD dimers. Note how the dephasing widths and transition energies span a smaller range for the B-QD dimers.

values of the widths of distributions of eigen exciton–exciton transition frequencies, $\bar{\sigma}_{mn}$, vary widely depending on the amount of correlation between the energies of the two eigen-excitons induced by the diagonalization of the intradot and interdot couplings. Pairs of highly mixed eigen-excitons will have smaller widths, $\bar{\sigma}_{mn}$, and longer dephasing times. In an isolated QD, this situation occurs for eigen-excitons within a given excitonic band because of the SO coupling. In dimers, transition frequencies between low and high excitonic bands resulting from the interdot Coulomb coupling, such as $1S^L_{3/2}$ and $1S^H_{3/2}$, $1S^L_{1/2}$ and $1S^H_{1/2}$, $2S^L_{3/2}$ and $2S^H_{3/2}$, and $2S^L_{1/2}$ and $2S^H_{1/2}$, will have longer dephasing times than interband transitions, for example, those involving $1S^L_{3/2}$ and $2S^H_{3/2}$. We show in Fig. 4 the values of $\bar{\omega}_{0m}$ and $\bar{\sigma}_{GS-m}$ computed using Eqs. (27) and (28) for ensembles of 2000 dimers with the size and dispersion of the ensemble studied in the experiments ($\bar{D}$ = 2.8 nm for S-QD and $\bar{D}$ = 3.5 nm for B-QD) both with 5% size dispersion. Note how the dephasing widths increase with the transition frequencies, $\bar{\omega}_{0m}$. In Fig. 4(a), one distinguishes four bands of eigen-excitons and their splittings due to the interdot Coulomb couplings. As discussed in Sec. II B, for the B-QD dimers [Fig. 4(b)], the two middle bands overlap.

The values of the inhomogeneous dephasing widths of the inter-exciton coherences, $\bar{\sigma}_{mn}$, (that contribute to the oscillating behavior along T in the 2D maps) are given in Figs. 4(c) and 4(d) for the S-QD and B-QD dimers, respectively. Inter-exciton coherences that involve eigen-excitons of the dimer with a high weight on 2S bands have larger dephasing widths (≈> 0.05 eV) than the ones involving 1S bands (≈0.02 eV–0.04 eV). As discussed above (Fig. 3), dimer eigen-excitons belonging to the 1S bands are significantly delocalized over the two dots so that the 1S inter-exciton coherences correspond to interdot beatings. Due to the high degree of correlation induced by the diagonalization of the interdot Coulomb coupling, some pairs of eigen-excitons, between fine structure states belonging to the same band, have smaller widths (<0.01 eV), with lifetimes in the hundreds of fs. On this time scale, these electronic coherences will be coupled to phonons and subject to dephasing processes due to interactions with the environment.

III. CHARACTERIZATION OF ELECTRONIC COHERENCES BY 2DES

We compare the results obtained using the modeling approach described in Sec. II with 2DES experimental data obtained on samples of interacting and non-interacting CdSe QDs. We considered two solid state samples prepared by a layer-by-layer deposition procedure as described in Refs. 37 and 62, starting from colloidal solutions of CdSe QDs with mean diameters of 2.8 nm (S-QD) and

3.5 nm (B-QD), respectively, with a zinc-blende crystal structure. The size dispersion for both samples has been estimated about 5% by TEM measurements.[37] Covalent links between dots have been promoted using 1,3-propanedithiol (PDT), having a nominal length of 0.55 nm; see Fig. 1(a). In these samples, it can be reasonably assumed that electronic coupling is established predominantly between pairs of QDs linked by dithiol ligands,[37,62–64] which supports modeling the response in terms of large ensembles of size-dispersed QD dimers. For comparison, a hexane solution of non-interacting B-QD dots has also been investigated to test the results of computations in the absence of interdot coupling, which in the modeling amounts to turning off the interdot Coulomb coupling, V_{inter}^{1S-1S}, V_{inter}^{2S-2S}, V_{inter}^{1S-2S} in Fig. 1(c). More details on the experimental sample properties can be found in the supplementary material.

For the comparison with experimental 2DES maps, we begin by discussing the assignment of excitonic bands in the absorption spectra computed for ensembles of S-QD and B-QD dimers since they determine the excitation (x axis, abscissa) and emission (y axis, ordinate) coordinates of the inter-exciton coherences in the 2D maps shown below. In first order perturbation theory, and in the weak pulse limit, using the results of Sec. II B [Eqs. (19), (27), and (28)], the absorption spectrum is given by

$$S_{abs}(\omega) = \sum_{m}^{N} \tilde{\mu}_{0m}^2 \exp\left(-\frac{(\omega-\tilde{\omega}_{0m})^2}{2\tilde{\sigma}_{0m}^2}\right). \tag{32}$$

We show in Fig. 5 the computed spectra together with the impulse spectrum of the Hamiltonian [Eq. (19)], $S_{imp}(\omega) = \sum_{m}^{M} \tilde{\mu}_{0m}^2 \delta(\omega-\tilde{\omega}_{0m})$, for the S-QD dimers [Fig. 5(a)] and B-QD ones [Fig. 5(b)]. For both dimers, the low $1S_{3/2}^L$ band appears as a shoulder in the absorption spectrum because the oscillator strength of these dimer states, which would be dark in a dimer of identical dots, is much smaller than that of the $1S_{3/2}^H$ states. As shown in Fig. 3, these two excitonic bands are highly delocalized over the two dots. While the $1S_{1/2}^L$–$1S_{1/2}^H$ and $2S_{3/2}^L$ and $2S_{3/2}^H$ bands overlap but can be resolved in the S-QD dimers [Fig. 5(a)], they cannot for the B-QD dimers [Fig. 5(b)]. $2S_{1/2}^L$ and $2S_{1/2}^H$ are clearly resolved, but they fall outside of the laser bandwidth, shown as a brown line. In the B-QD dimer, the laser pulse energy profile excites the entire 1S band and the low energy tail of the 2S one (essentially $2S_{3/2}^L$), while for the S-QD dimer, only the two lower 1S bands ($1S_{3/2}^L$ and $1S_{3/2}^H$) are excited, which makes the analysis of the 2D maps of this dimer more straightforward. The experimental spectral profiles[37] are shown in red. Overall, the 1S–2S gap is slightly underestimated in the model, more for the B-QD dimers than for the S-QD ones.[36,37] Since the laser bandwidth essentially does not allow to excite the 2S band in the S-QD sample and barely excites it in the B-QD one, the comparison between the experimental and the computed spectra is not affected by this discrepancy.

2DES measurements were performed using a passively phase-stabilized setup in the BOXCARS geometry as described in Refs. 36, 37, and 65. The laser spectral profile was tuned to cover as much as possible the main transitions of the samples, compatibly with the technical limitations of the laser source. The laser profile was centered at about 2.2 eV with a spectral width of about 0.5 eV (FWHM); see Fig. 5 above. The pulse duration, energy, and beam waist at the sample position were 9 fs, 7 nJ, and 100 μm, respectively. Additional details on the 2DES setup and experimental parameters can be found in Refs. 36 and 37 and in the supplementary material.

We show in Fig. 6 a comparison between the experimental and computed [Eq. (31)] 2D maps for the real part of the rephasing (photon echo) signal for S-QD [panel (a): computed; panel (b): experimental] and B-QD dimers [(c): computed; (d):

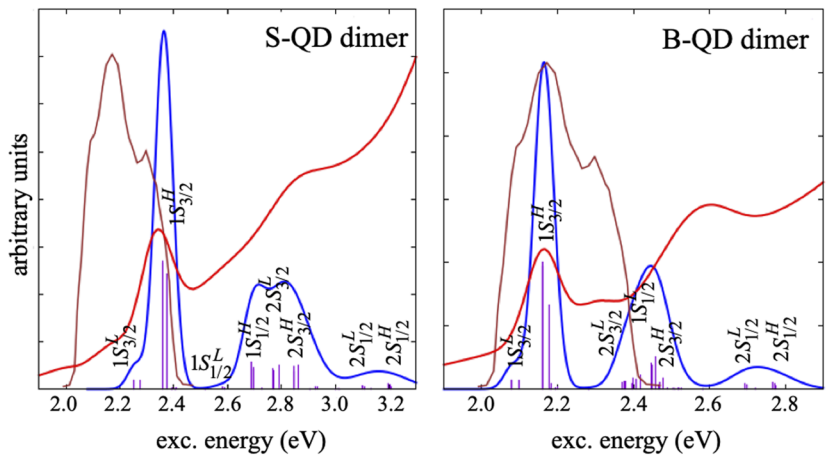

FIG. 5. Absorption spectra of the S-QD dimer [panel (a)] and of the B-QD dimer [(panel (b)]. The experimental laser pulse energy profile is shown in brown, the computed absorption profile is shown in blue [Eq. (32)], the stick spectrum is shown in violet, and the experimental spectrum is shown in red. The bands are labeled according to the two cases defined in Figs. 1(b) and 1(c), respectively. The transition frequencies from the GS to the excitons are slightly overestimated in the model. To allow a better comparison with the excitation and emission frequencies of the experimental 2D maps and a correct assignment of the states excited by the experimental laser profile, a red shift of GS-exciton frequencies of 0.09 eV has been applied to the S-QD dimer and one of 0.1 eV to the B-QD. Note that this overall shift does not affect the beating periods of the inter-exciton coherences.

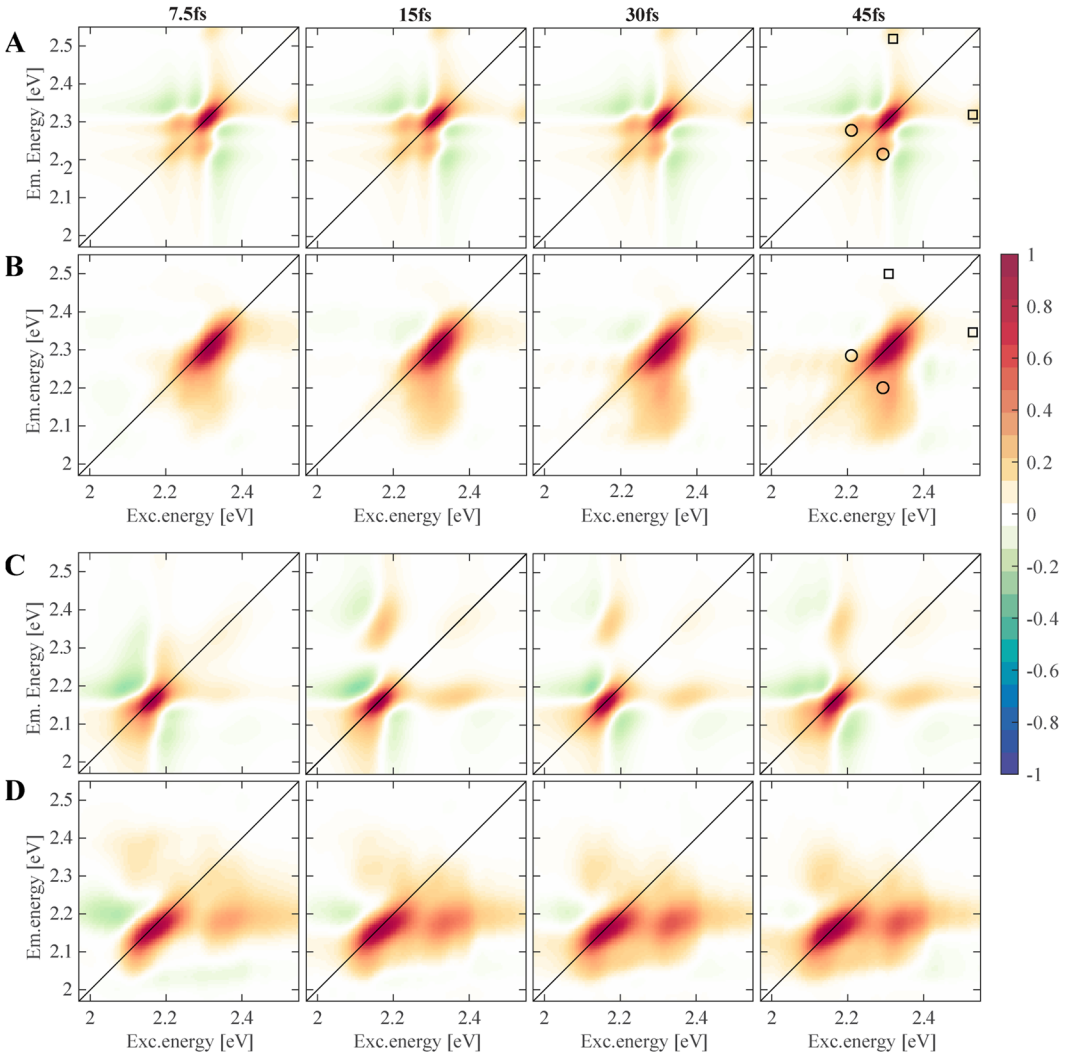

FIG. 6. Computed [(a) and (c)] and experimental [(b) and (d)] 2D maps (real part of the rephasing signal) for the S-QD dimers [(a) and (b)] and the B-QD dimers [(c) and (d)]. The four columns correspond to increasing values of the population time, T, as indicated. Maps are normalized to 1 on their maximum.

experimental] at increasing population times, T. Computed and experimental non-rephasing and purely absorptive maps are reported in the supplementary material (Figs. S3 and S4). The shape of the main signals in the experimental 2D maps [Figs. 6(b) and 6(d)] is strongly affected by the exciting laser profile because the final signal is the result of the convolution between the response function of the sample and the exciting electric fields.[43] Previous studies have shown that in the specific case of semiconducting QD, when both 1S and 2S fall in the laser bandwidth, the 2D experimental maps exhibit a square pattern, with two diagonal peaks and two cross peaks.[16,17,25,37,66,67] In Fig. 6, the diagonal signals are consistent with the addresses $(\tilde{\omega}_{0m}, \tilde{\omega}_{0m})$ and $(\tilde{\omega}_{0n}, \tilde{\omega}_{0n})$ and the cross peaks with addresses $(\tilde{\omega}_{0m}, \tilde{\omega}_{0n})$ and $(\tilde{\omega}_{0n}, \tilde{\omega}_{0m})$ identified for the eight GSB and SE paths contributing to the response function[Eq. (S5) of the supplementary material]. In our case, the laser profile covers only partially the 2S band (Fig. 5), especially in the case of S-QD sample, and therefore, the features associated with the high energy band are very weak. The cross-peak amplitudes directly depend on the oscillator strength of the two transitions, μ_{0m} and μ_{0n}, see Sec. II C, and on their spectral overlap with the laser pulse. The latter can also cause unequal cross-peak amplitude, especially in the case of a non-flat laser spectrum,[16] and this explains the slight asymmetry in the shape of the upper and lower cross peaks in the experimental maps [Figs. 6(b) and 6(d)]. 2DES measurements on solid state samples (colloidal QDs, quantum wells, transition metal chalcogenides, single crystals) are particularly challenging, as proven by the scarcity of works in the literature.[37,50,51,68–71] In the specific case of S-QD and B-QD samples, the presence of strong scattering effects and the low

values of absorbance significantly complicate the recording of the signal and its interpretation. One can notice small negative contributions in the experimental and computed 2D maps [Figs. 6(b) and 6(d)]. As discussed in Sec. II D, this negative signal is accounted for in the computed maps due to the causal character of the double Fourier transform in Eq. (30). Although ESA pathways might also contribute to these negative features, their contributions are negligible and are not included in the modeling.

Nonetheless, all considered, the agreement between the computed and experimental 2D maps is very good. In the case of the S-QD dimer [Figs. 6(a) and 6(b)], only the excitonic dimer bands $1S^L_{3/2}$ at ≈2.2 eV and the $1S^H_{3/2}$ at ≈2.3 eV are fully included in the laser bandwidth. The variations of the intensity of the cross-peak regions between these coordinates [pinpointed with circles in Figs. 6(a) and 6(b)] as a function of the population time are clearly seen in both the computed and experimental maps, with an increase from T = 7.5 fs to 30 fs and a decrease at 45 fs. Positions on the maps corresponding to the cross-peak regions oscillate with a period of 35 fs–40 fs, as shown in the traces plotted in Fig. 7(a). This period corresponds to electronic coherences between eigen-excitons belonging to the $1S^L_{3/2}$ and $1S^H_{3/2}$ bands, which are highly delocalized over the two dots [see Fig. 3(a) above]. The spacings between eigenstates belonging to each band are approximately twice the strength of the interdot Coulomb couplings (≈0.045 eV), as shown in Sec. II B.

There is also a correspondence between the low intensity cross peaks located in the computed maps at coordinates ≈(2.5–2.3) eV and (2.3–2.5) eV and experimental signals at the same positions [squares in Figs. 6(a) and 6(b)]. These signals correspond to coherences between dimer eigenstates of the $1S^H_{3/2}$ band and of the higher $1S^L_{1/2}$ band that falls on the blue edge of the laser bandwidth.

In the 2D maps of the B-QD dimer, in addition to a cross-peak region due to coherences between eigen-excitons of the $1S^L_{3/2}$ and $1S^H_{3/2}$ bands at ≈(2.2, 2.1) eV that is similar to the one seen in S-QD maps, one also observes clear cross-peak signals at (2.4–2.3) eV, which correspond to coherences between eigen-excitons of the $1S^H_{3/2}$ and the red part of the higher bands $2S^L_{3/2}$ and $1S^L_{1/2}$ [see Fig. 5(b)] that fall within the laser bandwidth. The $1S^L_{3/2}$–$1S^H_{3/2}$ coherences of B-QD in the (2.2, 2.1) eV region oscillate with a longer period (≈50 fs–60 fs), see Fig. 7(b), than the corresponding ones for S-QD [Fig. 7(a)] (≈35 fs–40 fs) as expected from the fact that the interdot Coulomb coupling strength is smaller (≈0.035 eV) for the B-QD dimers than for the S-QD ones. In the case of the B-QD dimers, in the same region of addresses, there is also a weaker contribution of intradot coherent beatings, as can be seen from Fig. 8.

In order to obtain a more global picture of the frequencies and dephasing times of the electronic coherences that can be excited in the laser bandwidth, we computed an inter-exciton coherence spectrum, which is defined as

$$S_{coh}(\omega, T) = \sum_{m,n>m}^{M} \tilde{\mu}^2_{0m}\tilde{\mu}^2_{0n} \exp\left(-\frac{(\omega - \tilde{\omega}_{mn})^2}{2\tilde{\sigma}^2_{mn}}\right) \exp\left(-\frac{\tilde{\sigma}^2_{mn}T^2}{2}\right), \tag{33}$$

where the range of excitons that contribute to the spectrum is limited to those experimentally accessed by the laser pulse. Experimentally, it is not possible to obtain the corresponding coherence spectrum retaining simultaneously both time and frequency resolution. Typically, the analysis of the coherent dynamics is performed Fourier transforming the beating traces along the population time: in this way, $S_{coh}(\omega)$ (the "Fourier spectrum") can be retrieved, but the dependence on T is lost. To keep both time and frequency resolution, we recently proposed a methodology based on bilinear time-frequency transforms.[72,73] This method is able to spread the signal information along both the time and frequency domains simultaneously, and it revealed to be extremely powerful in extracting higher-level information about the energetics and the dynamics of the coherent superposition of states.[37,74–76] However, this treatment is naturally limited by the time-frequency uncertainty, and therefore, its results must be evaluated with caution, especially when comparing with the ideal $S_{coh}(\omega, T)$ spectrum of Eq. (33).

To compare with the computed spectrum, the time traces along T at each (x, y) coordinate of the 2D maps have been analyzed with an optimized time-frequency bilinear transform (smoothed pseudo Wigner Ville transform, SPWV[72,73]). All time-frequency plots obtained at each (x, y) coordinate have then been averaged to provide a direct comparison with the theoretical spectrum of Eq. (33).

A comparison between the computed and experimental time-frequency plots of the coherence spectra is shown in Fig. 8, where the x axis is the coherence frequency [expressed in energy units (eV)

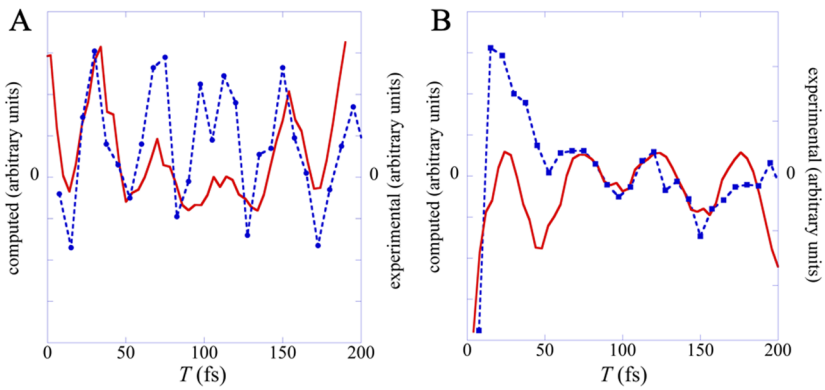

FIG. 7. Eigen-exciton coherences beating along T at a given address on the 2D maps shown in Fig. 6. Computed traces are shown in full line (red); experimental are shown in dashes (blue); the addresses on the 2D maps are given in parentheses. (a) S-QD dimer, computed: (2.30, 2.22) eV in Fig. 6(a), experimental: blue (2.37, 2.11) eV in Fig. 6(b). (b) B-QD dimer, computed: red (2.17, 2.10) in Fig. 6(c); experimental: blue (2.17, 2.04) eV in Fig. 6(d). Two more traces are shown in Fig. S5 of the supplementary material.

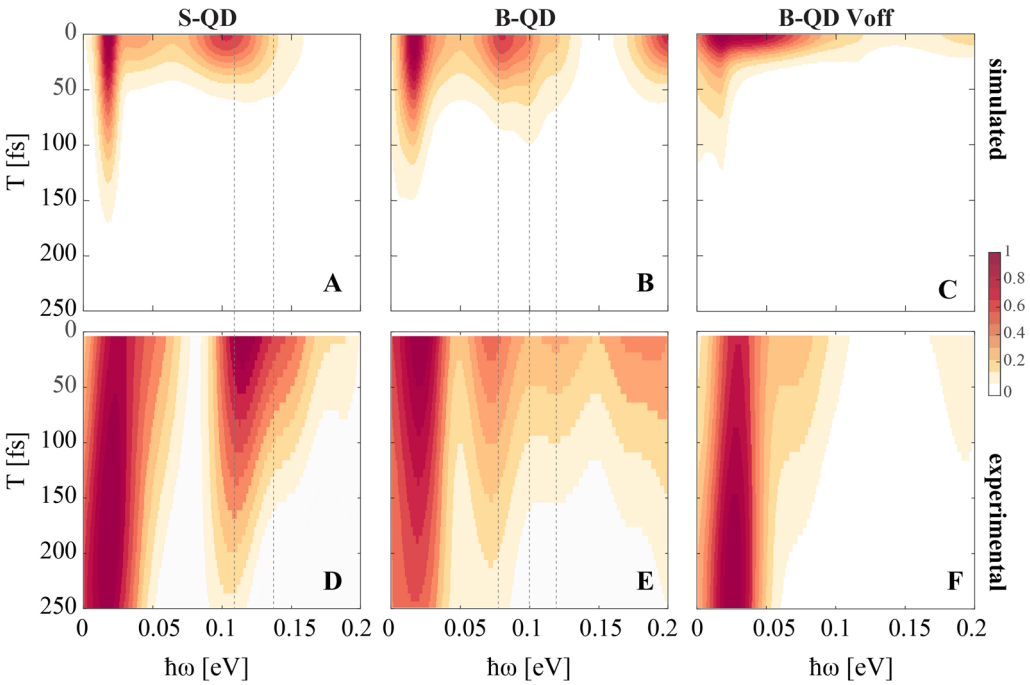

FIG. 8. Simulated (upper row) and experimental (lower row) coherence spectra for S-QD dimers [(a) and (d)], B-QD dimers [(b) and (e)], and B-QD non-interacting monomers [(c) and (f)]. The plots are normalized to 1 on their maximum. Dashed lines are traced at relevant values of beating frequency as a guide for the eye.

to directly compare with inter-exciton energy gaps] and the y axis is the population time T. The computed $S_{coh}(\omega, T)$ are shown in the first row, while the experimental ones are shown in the second one, respectively. Overall, the comparison is good, confirming the electronic character of the short time coherent dynamics in these samples. One can note that the experimental dephasing times appear systematically longer than the computed ones. This is due to the well-known numerical issues inherent in the application of time-frequency transforms and basically connected with the limitations due to time-frequency uncertainty.[72,77,78]

All plots exhibit a sharp peak at low frequencies (0.025 eV = 200 cm^{-1}). In the computed maps, these transition frequencies correspond to energy differences between FS states belonging to the same excitonic band. The FS electronic coherences between eigen-excitons delocalized over the two dots have rather long dephasing times (100 fs–200 fs) for S-QD and slightly longer for B-QD (150 fs–250 fs), as can be seen from Figs. 4(c) and 4(d), respectively. In the experimental maps, the signal at this frequency is a superposition of both FS states coherent superpositions and the contribution of the longitudinal (LO) phonon mode, falling at the same frequency and already well characterized in CdSe QDs.[17–21,23,25,79]

The LO phonon contribution and its possible mixing with electronic degrees of freedom[21,80–84] are not included in the purely electronic model that we use here since it is expected to contribute on a longer timescale.[37,42] This leads to a relatively more intense contribution of the signal at 0.025 eV in the experimental than in the computed maps and explains the growing trend as a function of the population time.

The signal arising from the interdot coherences between eigen-exciton states of the $1S^L_{3/2}$–$1S^H_{3/2}$ bands, highlighted in Fig. 7 at specific coordinates in the 2D maps, is clearly distinguishable in all panels. For S-QD dimers, the interdot coherence peak falls at transition frequencies of about 0.12 eV for both computed [Fig. 8(a)] and experimental [Fig. 8(d)] spectra, while it appears at slightly lower frequencies, in the range 0.08 eV–0.1 eV for B-QD dimers [Figs. 8(b) and 8(d)]. Remarkably, both theoretical and computed maps for B-QD dimers could capture the presence of more than one peak within this broadband, confirming the good correspondence between the simulation and experimental data. Different maxima in this spectral region correspond to different combinations of superpositions between states belonging to the $1S^L_{3/2}$–$1S^H_{3/2}$ bands. These peaks appear as shoulders in the experimental S-QD [Fig. 8(d)] and are not resolved in the computed one [Fig. 8(a)]. One can see by comparing Figs. 4(c) and 4(d) that, indeed, the computed dephasing widths for the inter-exciton coherences in the range ≈0.1 eV–0.12 eV for the S-QD dimer are larger than those in the ≈0.08 eV–0.1 eV range for the B-QD dimers.

For the B-QD dimers, one also distinguishes a band of coherences at a higher energy, starting from 0.20 eV. This band corresponds to coherences between 1S and 2S excitons, which in the dimer correspond to the $1S^H_{3/2}$ and $2S^L_{3/2}$–$1S^L_{1/2}$ eigen-exciton states [see Fig. 5(b)]. For isolated B-QDs, the peak corresponding to inter-band 1S–2S electronic coherences above 0.2 eV is also clearly visible, as shown in Figs. 8(c) and 8(f). This interband intradot beating was already reported in Ref. 36. In Fig. 8(c), the computed coherence spectrum was obtained by turning off the interdot Coulomb

coupling in the Hamiltonian matrix shown in Fig. 1(b), which corresponds to an ensemble of 4000 non-interacting B-QDs. Figure 8(f) shows the experimental coherence spectra for isolated QDs of a size equivalent to that of the B-QDs within the 5% size dispersion ($\bar{D}$ = 3.7 nm) in water. In addition, by comparing Figs. 8(b) and 8(c) and Figs. 8(e) and 8(f), one clearly sees the difference between the electronically coupled and non-interacting B-QDs in the 0.08 eV–0.1 eV region. The interdot coherence signature appears as a clear broad peak with the substructure discussed above in Fig. 8(b), while there is only a low intensity background contribution in the region of interdot coherence frequencies for the isolated B-QDs in Fig. 8(c). Note that as discussed in Ref. 37, the overlap between the intradot and interdot coherences is less pronounced for S-QD dimers because the frequencies of the interdot coherences in the case of the S-QD dimer is higher in energy.

IV. CONCLUDING REMARKS

Our joint experimental–theoretical study shows that it is possible to characterize the fast beating electronic coherences in colloidal QD solids at room temperature by 2D electronic spectroscopy. These electronic coherences exhibit periodic beatings for a time of ≈100 fs, long enough to be identified at specific absorption–emission addresses on 2D frequency maps.

We have recently suggested exploiting these electronic coherences in a solid state quantum dot device to emulate the nuclear quantum dynamics of two coupled oscillators.[14] Beyond this and other potential applications to quantum information processing, electronically coupled colloidal QD solids and their coherent nonlinear optical response at room temperature could be exploited in a broad range of applications from photonic and quantum devices to energy and charge transport operations and, in general, for all applications where a strict control of the time evolution of the electronic properties after photoexcitation is required.

Characterizing the time evolution of coherent superpositions of states in the ultrafast time domain is crucial not only to understand the mechanisms of dephasing but also to harness the quantum nature of the coherent phenomena. The characterization of coherent dynamics in QD materials, the identification of their physical origin and the factors contributing to their dephasing dynamics, will allow for a more reliable design of QD based devices.

In this work, we have proved, on the experimental side, that it is possible to identify and follow the time evolution of coherent superpositions of electronic states optically generated in samples of interacting QDs (QD dimers in the solid state). Theoretical simulation tools have been set, which are able to provide a rigorous interpretation of the experimental results and clearly distinguish between the contributions of different coherent electronic beatings. These tools allow distinguishing intradot and interdot coherent electronic dynamics, opening up the possibility of designing and engineering strongly interacting QD systems, and exploiting more systematically their quantum properties. The role of size, interdot distance, and inhomogeneous size distributions on the electronic properties and (coherent) dynamics has been systematically investigated, providing important guidelines for the choice of future materials to be employed in QD based devices.

SUPPLEMENTARY MATERIAL

See the supplementary material for more details on the model used in this work, additional figures, and the description of the experimental setup.

ACKNOWLEDGMENTS

This work was financially supported by the H2020 FET Project COPAC (Grant No. 766563). E.C. also acknowledges partial support from the MIUR PRIN 2015 (Grant No. 2015XBZ5YA). F.R. and H.G. acknowledge the support from the Consortium des Equipements de Calcul Intensif (CECI), funded by the FRS-FNRS (Fonds National de la recherche Scientifique, Belgium) under Grant No. 2.5020.11 for the computations. F.R. also acknowledges partial support from the FRS-FNRS through Grant Nos. J.0012.18 and T.0205.20. We thank Marinella Striccoli (CNR IPCF, Bari) and Yossi Paltiel (The Hebrew University of Jerusalem) for providing the QD materials and for useful discussions.

DATA AVAILABILITY

The data that support the findings of this study are available from the corresponding author upon reasonable request.

REFERENCES

[1] *Nanocrystal Quantum Dots*, edited by V. I. Klimov (CRC Press, Boca Raton, 2010).
[2] L. E. Brus, "Electron–electron and electron-hole interactions in small semiconductor crystallites: The size dependence of the lowest excited electronic state," J. Chem. Phys. **80**(9), 4403–4409 (1984).
[3] A. P. Alivisatos, "Semiconductor clusters, nanocrystals, and quantum dots," Science **271**(5251), 933 (1996).
[4] D. J. Norris and M. G. Bawendi, "Measurement and assignment of the size-dependent optical spectrum in CdSe quantum dots," Phys. Rev. B **53**(24), 16338–16346 (1996).
[5] K. Tvrdy, P. A. Frantsuzov, and P. V. Kamat, "Photoinduced electron transfer from semiconductor quantum dots to metal oxide nanoparticles," Proc. Natl. Acad. Sci. U. S. A. **108**, 29 (2011).
[6] *Colloidal Quantum Dot Optoelectronics and Photovoltaics*, edited by G. Konstantatos and E. Sargent (Cambridge University Press, Cambridge, 2013).
[7] C. R. Kagan, E. Lifshitz, E. H. Sargent, and D. V. Talapin, "Building devices from colloidal quantum dots," Science **353**(6302), aac5523 (2016).
[8] O. V. Kozlov, Y.-S. Park, J. Roh, I. Fedin, T. Nakotte, and V. I. Klimov, "Sub–single-exciton lasing using charged quantum dots coupled to a distributed feedback cavity," Science **365**(6454), 672 (2019).
[9] Y. E. Panfil, M. Oded, and U. Banin, "Colloidal quantum nanostructures: Emerging materials for display applications," Angew. Chem. **57**(16), 4274–4295 (2018).
[10] A. Imamoglu, D. D. Awschalom, G. Burkard, D. P. DiVincenzo, D. Loss, M. Sherwin, and A. Small, "Quantum information processing using quantum dot spins and cavity QED," Phys. Rev. Lett. **83**(20), 4204–4207 (1999).
[11] D. Loss and D. P. DiVincenzo, "Quantum computation with quantum dots," Phys. Rev. A **57**(1), 120–126 (1998).
[12] B. Fresch, M. Cipolloni, T.-M. Yan, E. Collini, R. D. Levine, and F. Remacle, "Parallel and multivalued logic by the two-dimensional photon-echo response of a rhodamine–DNA complex," J. Phys. Chem. Lett. **6**, 1714–1718 (2015).
[13] B. Fresch, D. Hiluf, E. Collini, R. D. Levine, and F. Remacle, "Molecular decision trees realized by ultrafast electronic spectroscopy," Proc. Natl. Acad. Sci. U. S. A. **110**(43), 17183–17188 (2013).

[14]K. Komarova, H. Gattuso, R. D. Levine, and F. Remacle, "Quantum device emulates the dynamics of two coupled oscillators," J. Phys. Chem. Lett. **11**, 6990–6995 (2020).
[15]E. Cassette, R. D. Pensack, B. Mahler, and G. D. Scholes, "Room-temperature exciton coherence and dephasing in two-dimensional nanostructures," Nat. Commun. **6**, 6086 (2015).
[16]E. Cassette, J. C. Dean, and G. D. Scholes, "Two-dimensional visible spectroscopy for studying colloidal semiconductor nanocrystals," Small **12**(16), 2234–2244 (2016).
[17]D. B. Turner, Y. Hassan, and G. D. Scholes, "Exciton superposition states in CdSe nanocrystals measured using broadband two-dimensional electronic spectroscopy," Nano Lett. **12**(2), 880–886 (2012).
[18]J. R. Caram, H. Zheng, P. D. Dahlberg, B. S. Rolczynski, G. B. Griffin, D. S. Dolzhnikov, D. V. Talapin, and G. S. Engel, "Exploring size and state dynamics in CdSe quantum dots using two-dimensional electronic spectroscopy," J. Chem. Phys. **140**(8), 084701 (2014).
[19]J. R. Caram, H. Zheng, P. D. Dahlberg, B. S. Rolczynski, G. B. Griffin, A. F. Fidler, D. S. Dolzhnikov, D. V. Talapin, and G. S. Engel, "Persistent interexcitonic quantum coherence in CdSe quantum dots," J. Phys. Chem. Lett. **5**(1), 196–204 (2014).
[20]S. Palato, H. Seiler, P. Nijjar, O. Prezhdo, and P. Kambhampati, "Atomic fluctuations in electronic materials revealed by dephasing," Proc. Natl. Acad. Sci. U. S. A. **117**, 11940 (2020).
[21]S. Dong, D. Trivedi, S. Chakrabortty, T. Kobayashi, Y. Chan, O. V. Prezhdo, and Z.-H. Loh, "Observation of an excitonic quantum coherence in CdSe nanocrystals," Nano Lett. **15**(10), 6875–6882 (2015).
[22]P. Kambhampati, "Unraveling the structure and dynamics of excitons in semiconductor quantum dots," Acc. Chem. Res. **44**(1), 1–13 (2011).
[23]T. A. Gellen, J. Lem, and D. B. Turner, "Probing homogeneous line broadening in CdSe nanocrystals using multidimensional electronic spectroscopy," Nano Lett. **17**(5), 2809–2815 (2017).
[24]D. J. Trivedi, L. Wang, and O. V. Prezhdo, "Auger-mediated electron relaxation is robust to deep hole traps: Time-domain *ab initio* study of CdSe quantum dots," Nano Lett. **15**, 2086–2091 (2015).
[25]M. Righetto, L. Bolzonello, A. Volpato, G. Amoruso, A. Panniello, E. Fanizza, M. Striccoli, and E. Collini, "Deciphering hot- and multi-exciton dynamics in core–shell QDs by 2D electronic spectroscopies," Phys. Chem. Chem. Phys. **20**(27), 18176–18183 (2018).
[26]H. Seiler, S. Palato, C. Sonnichsen, H. Baker, and P. Kambhampati, "Seeing multiexcitons through sample inhomogeneity: Band-edge biexciton structure in CdSe nanocrystals revealed by two-dimensional electronic spectroscopy," Nano Lett. **18**(5), 2999–3006 (2018).
[27]C. Lin, K. Gong, D. F. Kelley, and A. M. Kelley, "Size-dependent exciton–phonon coupling in CdSe nanocrystals through resonance Raman excitation profile analysis," J. Phys. Chem. C **119**(13), 7491–7498 (2015).
[28]O. V. Prezhdo, "Photoinduced dynamics in semiconductor quantum dots: Insights from time-domain *ab initio* studies," Acc. Chem. Res. **42**(12), 2005–2016 (2009).
[29]N. Lenngren, M. A. Abdellah, K. Zheng, M. J. Al-Marri, D. Zigmantas, K. Žídek, and T. Pullerits, "Hot electron and hole dynamics in thiol-capped CdSe quantum dots revealed by 2D electronic spectroscopy," Phys. Chem. Chem. Phys. **18**(37), 26199–26204 (2016).
[30]A. L. Efros and M. Rosen, "The electronic structure of semi-conducting nanocrystal," Annu. Rev. Mater. Sci. **30**, 475–521 (2000).
[31]P. C. Sercel and A. L. Efros, "Band-edge exciton in CdSe and other II–VI and III–V compound semiconductor nanocrystals—Revisited," Nano Lett. **18**(7), 4061–4068 (2018).
[32]J. Kim, C. Y. Wong, and G. D. Scholes, "Exciton fine structure and spin relaxation in semiconductor colloidal quantum dots," Acc. Chem. Res. **42**(8), 1037–1046 (2009).
[33]C. Y. Wong and G. D. Scholes, "Using two-dimensional photon echo spectroscopy to probe the fine structure of the ground state biexciton of CdSe nanocrystals," J. Lumin. **131**(3), 366–374 (2011).
[34]H. Ma, Z. Jin, Z. Zhang, G. Li, and G. Ma, "Exciton spin relaxation in colloidal CdSe quantum dots at room temperature," J. Phys. Chem. A **116**(9), 2018–2023 (2012).
[35]V. M. Huxter, V. Kovalevskij, and G. D. Scholes, "Dynamics within the exciton fine structure of colloidal CdSe quantum dots," J. Phys. Chem. B **109**(43), 20060–20063 (2005).
[36]E. Collini, H. Gattuso, L. Bolzonello, A. Casotto, A. Volpato, C. N. Dibenedetto, E. Fanizza, M. Striccoli, and F. Remacle, "Quantum phenomena in nanomaterials: Coherent superpositions of fine structure states in CdSe nanocrystals at room temperature," J. Phys. Chem. C **123**, 31286–31293 (2019).
[37]E. Collini, H. Gattuso, Y. Kolodny, L. Bolzonello, A. Volpato, H. T. Fridman, S. Yochelis, M. Mor, J. Dehnel, E. Lifshitz, Y. Paltiel, R. D. Levine, and F. Remacle, "Room-temperature inter-dot coherent dynamics in multilayer quantum dot materials," J. Phys. Chem. C **124**(29), 16222–16231 (2020).
[38]H. Gattuso, R. D. Levine, and F. Remacle, "Massively parallel classical logic via coherent dynamics of an ensemble of quantum systems with dispersion in size," Proc. Natl. Acad. Sci. U. S. A. **117**(35), 21022 (2020).
[39]J. M. Luttinger and W. Kohn, "Motion of electrons and holes in perturbed periodic fields," Phys. Rev. **97**(4), 869–883 (1955).
[40]A. L. Efros, M. Rosen, M. Kuno, M. Nirmal, D. J. Norris, and M. Bawendi, "Band-edge exciton in quantum dots of semiconductors with a degenerate valence band: Dark and bright exciton states," Phys. Rev. B **54**(7), 4843–4856 (1996).
[41]C. Y. Wong and G. D. Scholes, "Biexcitonic fine structure of CdSe nanocrystals probed by polarization-dependent two-dimensional photon echo spectroscopy," J. Phys. Chem. A **115**(16), 3797–3806 (2011).
[42]H. Gattuso, B. Fresch, R. D. Levine, and F. Remacle, "Coherent exciton dynamics in ensembles of size-dispersed CdSe quantum dot dimers probed via ultrafast spectroscopy: A quantum computational study," Appl. Sci. **10**(4), 1328 (2020).
[43]S. Mukamel, *Principle of Non-Linear Optical Spectroscopy* (Oxford University Press, Oxford, 1995).
[44]P. Hamm and M. T. Zanni, *Concepts and Methods of 2D Infrared Spectroscopy* (Cambridge University Press, Cambridge, 2011).
[45]M. Cho, *Two-Dimensional Optical Spectroscopy* (CRC Press, Boca Raton, 2009).
[46]A. M. Brańczyk, D. B. Turner, and G. D. Scholes, "Crossing disciplines—A view on two-dimensional optical spectroscopy," Ann. Phys. **526**(1-2), 31–49 (2014).
[47]J. Jasieniak, M. Califano, and S. E. Watkins, "Size-dependent valence and conduction band-edge energies of semiconductor nanocrystals," ACS Nano **5**(7), 5888–5902 (2011).
[48]C. Y. Wong, J. Kim, P. S. Nair, M. C. Nagy, and G. D. Scholes, "Relaxation in the exciton fine structure of semiconductor nanocrystals," J. Phys. Chem. C **113**(3), 795–811 (2009).
[49]V. I. Klimov, "Optical nonlinearities and ultrafast carrier dynamics in semiconductor nanocrystals," J. Phys. Chem. B **104**(26), 6112–6123 (2000).
[50]C. R. Hall, J. O. Tollerud, H. M. Quiney, and J. A. Davis, "Three-dimensional electronic spectroscopy of excitons in asymmetric double quantum wells," New J. Phys. **15**(4), 045028 (2013).
[51]J. A. Davis, C. R. Hall, L. V. Dao, K. A. Nugent, H. M. Quiney, H. H. Tan, and C. Jagadish, "Three-dimensional electronic spectroscopy of excitons in asymmetric double quantum wells," J. Chem. Phys. **135**(4), 044510 (2011).
[52]K. Hyeon-Deuk and O. V. Prezhdo, "Multiple exciton generation and recombination dynamics in small Si and CdSe quantum dots: An *ab initio* time-domain study," ACS Nano **6**(2), 1239–1250 (2012).
[53]J. D. Hybl, A. W. Albrecht, S. M. Gallagher Faeder, and D. M. Jonas, "Two-dimensional electronic spectroscopy," Chem. Phys. Lett. **297**(3), 307–313 (1998).
[54]*The Unitary Group for the Evaluation of the Electronic Energy Matrix Elements*, Lecture Notes in Chemistry Vol. 22, edited by J. Hinze (Springer-Verlag, Berlin, 1981).
[55]Y. Alhassid and R. D. Levine, "Connection between the maximal entropy and the scattering theoretic analyses of collision processes," Phys. Rev. A **18**(1), 89–116 (1978).
[56]S. V. Kilina, D. S. Kilin, and O. V. Prezhdo, "Breaking the phonon bottleneck in PbSe and CdSe quantum dots: Time-domain density functional theory of charge carrier relaxation," ACS Nano **3**(1), 93–99 (2009).
[57]J. Cui, A. P. Beyler, I. Coropceanu, L. Cleary, T. R. Avila, Y. Chen, J. M. Cordero, S. L. Heathcote, D. K. Harris, O. Chen, J. Cao, and M. G. Bawendi, "Evolution of the single-nanocrystal photoluminescence linewidth with size and shell: Implications for exciton–phonon coupling and the optimization of spectral linewidths," Nano Lett. **16**(1), 289–296 (2016).

[58]M. R. Salvador, M. W. Graham, and G. D. Scholes, "Exciton-phonon coupling and disorder in the excited states of CdSe colloidal quantum dots," J. Chem. Phys. **125**(18), 184709 (2006).
[59]L. J. McKimmie, C. N. Lincoln, J. Jasieniak, and T. A. Smith, "Three-pulse photon echo peak shift measurements of capped CdSe quantum dots," J. Phys. Chem. C **114**(1), 82–88 (2010).
[60]L. Valkunas, D. Abramavicius, and T. Mancal, *Molecular Excitation Dynamics and Relaxation: Quantum Theory and Spectroscopy* (Wiley-VCH, Weinhem, 2013).
[61]A. Volpato, L. Bolzonello, E. Meneghin, and E. Collini, "Global analysis of coherence and population dynamics in 2D electronic spectroscopy," Opt. Express **24**(21), 24773–24785 (2016).
[62]E. Cohen, P. Komm, N. Rosenthal-Strauss, J. Dehnel, E. Lifshitz, S. Yochelis, R. D. Levine, F. Remacle, B. Fresch, G. Marcus, and Y. Paltiel, "Fast energy transfer in CdSe quantum dot layered structures: Controlling coupling with covalent-bond organic linkers," J. Phys. Chem. C **122**(10), 5753–5758 (2018).
[63]E. Cohen, I. Gdor, E. Romero, S. Yochelis, R. van Grondelle, and Y. Paltiel, "Achieving exciton delocalization in quantum dot aggregates using organic linker molecules," J. Phys. Chem. Lett. **8**(5), 1014–1018 (2017).
[64]E. Cohen, M. Gruber, E. Romero, S. Yochelis, R. van Grondelle, and Y. Paltiel, "Properties of self-assembled hybrid organic molecule/quantum dot multilayered structures," J. Phys. Chem. C **118**(44), 25725–25730 (2014).
[65]L. Bolzonello, A. Volpato, E. Meneghin, and E. Collini, "Versatile setup for high-quality rephasing, non-rephasing, and double quantum 2D electronic spectroscopy," J. Opt. Soc. Am. B **34**(6), 1223–1233 (2017).
[66]Y. Kobayashi, C.-H. Chuang, C. Burda, and G. D. Scholes, "Exploring ultrafast electronic processes of quasi-type II nanocrystals by two-dimensional electronic spectroscopy," J. Phys. Chem. C **118**(29), 16255–16263 (2014).
[67]G. B. Griffin, S. Ithurria, D. S. Dolzhnikov, A. Linkin, D. V. Talapin, and G. S. Engel, "Two-dimensional electronic spectroscopy of CdSe nanoparticles at very low pulse power," J. Chem. Phys. **138**(1), 014705 (2013).
[68]K. W. Stone, K. Gundogdu, D. B. Turner, X. Li, S. T. Cundiff, and K. A. Nelson, "Two-quantum 2D FT electronic spectroscopy of biexcitons in GaAs quantum wells," Science **324**(5931), 1169 (2009).
[69]D. B. Turner and K. A. Nelson, "Coherent measurements of high-order electronic correlations in quantum wells," Nat **466**(7310), 1089–1092 (2010).
[70]K. Hao, L. Xu, P. Nagler, A. Singh, K. Tran, C. K. Dass, C. Schüller, T. Korn, X. Li, and G. Moody, "Coherent and incoherent coupling dynamics between neutral and charged excitons in monolayer $MoSe_2$," Nano Lett. **16**(8), 5109–5113 (2016).
[71]A. E. Böhmer, F. Hardy, F. Eilers, D. Ernst, P. Adelmann, P. Schweiss, T. Wolf, and C. Meingast, "Lack of coupling between superconductivity and orthorhombic distortion in stoichiometric single-crystalline FeSe," Phys. Rev. B **87**(18), 180505 (2013).
[72]A. Volpato and E. Collini, "Time-frequency methods for coherent spectroscopy," Opt. Express **23**(15), 20040–20050 (2015).
[73]A. Volpato and E. Collini, "Optimization and selection of time-frequency transforms for wave-packet analysis in ultrafast spectroscopy," Opt. Express **27**(3), 2975–2987 (2019).
[74]E. Romero, J. Prior, A. W. Chin, S. E. Morgan, V. I. Novoderezhkin, M. B. Plenio, and R. van Grondelle, "Quantum–coherent dynamics in photosynthetic charge separation revealed by wavelet analysis," Sci. Rep. **7**(1), 2890 (2017).
[75]E. Meneghin, A. Volpato, L. Cupellini, L. Bolzonello, S. Jurinovich, V. Mascoli, D. Carbonera, B. Mennucci, and E. Collini, "Coherence in carotenoid-to-chlorophyll energy transfer," Nat. Commun. **9**(1), 3160 (2018).
[76]J. D. Gaynor, J. Sandwisch, and M. Khalil, "Vibronic coherence evolution in multidimensional ultrafast photochemical processes," Nat. Commun. **10**(1), 5621 (2019).
[77]Q. Shie and C. Dapang, "Joint time-frequency analysis," IEEE Signal Process. Mag. **16**(2), 52–67 (1999).
[78]K. Gröchenig, *Foundations of Time-Frequency Analysis* (Birkhäuser, Boston, 2001).
[79]P. Kambhampati, "Hot exciton relaxation dynamics in semiconductor quantum dots: Radiationless transitions on the nanoscale," J. Phys. Chem. C **115**(45), 22089–22109 (2011).
[80]A. M. Kelley, "Electron–phonon coupling in CdSe nanocrystals," J. Phys. Chem. Lett. **1**(9), 1296–1300 (2010).
[81]A. Liu, D. B. Almeida, W. K. Bae, L. A. Padilha, and S. T. Cundiff, "Non-markovian exciton-phonon interactions in core-shell colloidal quantum dots at femtosecond timescales," Phys. Rev. Lett. **123**(5), 057403 (2019).
[82]A. M. Kelley, "Exciton-optical phonon coupling in II-VI semiconductor nanocrystals," J. Chem. Phys. **151**(14), 140901 (2019).
[83]S. Pal, D. J. Trivedi, A. V. Akimov, B. Aradi, T. Frauenheim, and O. V. Prezhdo, "Nonadiabatic molecular dynamics for thousand atom systems: A tight-binding approach toward PYXAID," J. Chem. Theory Comput. **12**(4), 1436–1448 (2016).
[84]J. Seibt and T. Pullerits, "Beating signals in 2D spectroscopy: Electronic or nuclear coherences? Application to a quantum dot model system," J. Phys. Chem. C **117**(36), 18728–18737 (2013).